

# Mechanics of Crystalline Nanowires: An Experimental Perspective

**Yong Zhu**

Department of Mechanical  
and Aerospace Engineering,  
North Carolina State University,  
Raleigh, NC 27502  
e-mail: yong\_zhu@ncsu.edu

*A wide variety of crystalline nanowires (NWs) with outstanding mechanical properties have recently emerged. Measuring their mechanical properties and understanding their deformation mechanisms are of important relevance to many of their device applications. On the other hand, such crystalline NWs can provide an unprecedented platform for probing mechanics at the nanoscale. While challenging, the field of experimental mechanics of crystalline nanowires has emerged and seen exciting progress in the past decade. This review summarizes recent advances in this field, focusing on major experimental methods using atomic force microscope (AFM) and electron microscopes and key results on mechanics of crystalline nanowires learned from such experimental studies. Advances in several selected topics are discussed including elasticity, fracture, plasticity, and anelasticity. Finally, this review surveys some applications of crystalline nanowires such as flexible and stretchable electronics, nanocomposites, nanoelectromechanical systems (NEMS), energy harvesting and storage, and strain engineering, where mechanics plays a key role. [DOI: 10.1115/1.4035511]*

## 1 Introduction

With the advance of nanotechnology, a plethora of nanostructures such as zero-dimensional (0D) structures like nanoparticles, one-dimensional (1D) structures like nanotubes, nanowires (NWs), and nanofibers, and two-dimensional (2D) materials like graphene and transition metal dichalcogenide monolayers have emerged. Numerous studies have reported that these nanostructures typically possess ultrahigh mechanical strengths, close to their ideal strengths [1,2]. Among them, 1D nanostructures have been used as building blocks for a wide range of applications including nanoelectronics, nanosensors, nanocomposites, energy harvesting/storage, and nanoelectromechanical systems (NEMS). For example, carbon nanotubes (CNTs) have been used in conductive and high-strength composites [3,4]. ZnO NWs have been demonstrated to harvest mechanical energy through piezoelectric effect [5] and used in highly efficient dye-sensitized solar cells [6]. Si NWs have been used to harvest waste heat using thermoelectric effect [7] and can potentially serve as an excellent class of materials as anodes in lithium-ion batteries [8]. SiC NWs have been used in ultrahigh-frequency nanoresonators with high-quality factor [9]. Ag NWs are outstanding conductors and have been successfully used in flexible, transparent electrodes [10,11] and stretchable electrodes [12–14].

It is known that material properties can change with elastic strain including electronic band gap, carrier mobility, phononic band gap, thermal transport, ferroic transition, catalytic activity, etc. Hence, the ultrahigh strength offers an unprecedented opportunity to tune the properties of crystalline NWs through the elastic strain engineering [1]. For example, for Si NWs the electron–hole recombination rate can increase sixfold under a strain of 5% [15]; for Ag NWs, axial or bending strain was found to significantly affect the surface plasmon resonance [16,17]. For device applications including elastic strain engineering, it is of critical relevance to *measure, understand, and eventually design mechanical properties of 1D nanostructures.*

Mechanical properties of materials at the nanoscale significantly deviate from their bulk counterparts. This is true not only for nanostructured materials (e.g., nanocrystalline or nanotwinned materials) but also for nanostructures (surface-dominated structures like NWs). Nanoindentation on bulk crystals or thin films is a well-characterized technique for probing mechanics at the nanometer length scale [18,19], manifesting so-called indentation size effects, i.e., an increase in hardness with decreasing depth of penetration [20]. However, nanoindentation introduces complicated stress state and is ineffective in evaluating the effect of free surfaces on mechanical properties. In the past decade, mechanical properties under uniaxial loading (e.g., using micro/nanopillars with diameters well above 100 nm) have received significant interests, manifesting another type of size effects—“smaller is stronger” (an increase in strength with decreasing diameter) [21–25]. A plethora of theories were proposed to explain the observed size effects; a now commonly accepted theory hypothesizes that in such pillars the dislocations multiply and form complex networks through the operation of single-arm sources as supported by dislocation dynamics simulations [22,26–29] and in situ transmission electron microscopy (TEM) observations [30]. With further shrinkage of the size into the regime where surface effects become dominant (e.g.,  $\sim 100$  nm or below), NWs have received much interest. The NWs often exhibit near ideal strength. Metal NWs tend to deform via dislocation nucleation at the surface, glide, and subsequent annihilation at the free surfaces as supported by molecular dynamics (MD) simulations [31–33] and in situ TEM observations [34].

In this review, we provide a summary of recent advances in mechanics of crystalline NWs focusing on the experimental aspects. Mechanics of carbon nanotubes has been well reviewed [35], while modeling on mechanics of crystalline NWs has been an extremely active field in the last decade or so and deserves its own review articles [1,36,37]. This review is organized as follows: In Sec. 2, we summarize major experimental methods to measure mechanical behaviors of NWs employing tools such as atomic force microscope (AFM) and electron microscopes. While this review is limited to crystalline NWs, these experimental methods can be readily applied to other 1D nanostructures such as amorphous NWs, nanotubes, and nanofibers. In Sec. 3, we discuss a

Manuscript received June 24, 2016; final manuscript received December 11, 2016; published online January 12, 2017. Assoc. Editor: Xiaodong Li.

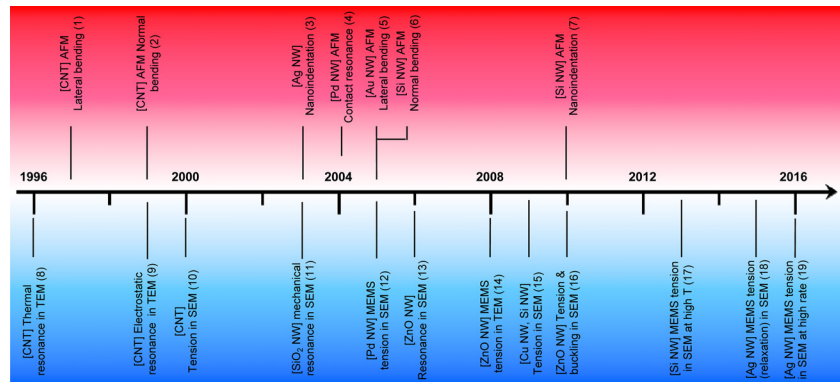


**Fig. 1** Key developments in the experimental methods for measuring mechanical properties of 1D nanostructures including CNTs and crystalline NWs in the last two decades. 1: AFM lateral bending [38], 2: AFM normal bending [39], 3: nanoindentation [40], 4: AFM contact resonance [41], 5: AFM lateral bending [42], 6: AFM normal bending [43], 7: AFM nanoindentation [44], 8: thermal resonance in TEM [45], 9: electrostatic resonance in TEM [46], 10: tension in SEM [47], 11: mechanical resonance in SEM [48], 12: MEMS tension in SEM [49], 13: resonance in SEM [50], 14: MEMS tension in TEM [98], 15: tension in SEM [51,52], 16: tension and bending in SEM [53], 17: MEMS tension in SEM at high temperature [54], 18: MEMS tension (relaxation) in SEM [55], and 19: MEMS tension in SEM at high strain rate [56]

number of mechanics topics of crystalline NWs including elasticity, fracture, plasticity, and anelasticity. In Sec. 4, we survey some mechanical applications of crystalline NWs ranging from stretchable electronics to energy applications to strain engineering. Before closing, challenges and future prospects of experimental mechanics of crystalline NWs are discussed.

## 2 Experimental Methods

Mechanical testing of 1D nanostructures has seen significant progress but remains challenging due to the fact that their diameters are typically less than 100 nm and lengths  $\sim 10 \mu\text{m}$ . Apart from a few specific methods, most testing methods involve tension or bending loading mode. The available testing methods can be mainly grouped into two categories based on the instruments involved: AFM/nanoindentation testing and electron microscopy testing. Figure 1 lists the key developments in the testing methods

for 1D nanostructures in these two categories in the past two decades (most of these methods are first of their kinds).

A fundamental difference exists between AFM/nanoindenter and electron microscopes—AFM or nanoindenter is an instrumented testing tool in addition to being an imaging tool, while an electron microscope is an imaging tool only. For AFM/nanoindentation testing of 1D nanostructures, the imaging capability is used to locate the position for testing followed with the testing capability. AFM/nanoindenter is limited as the “imaging” is realized by touching the samples, in analogy to the blind. AFM/nanoindentation testing employs commercially available instruments to apply load and measure deformation. During the mechanical testing, AFM or nanoindenter cannot perform the in situ imaging simultaneously but can be easily switched to the imaging mode before or after the mechanical testing.

For electron microscopy testing, a separate mechanical testing tool must be employed inside the electron microscope, which is often custom made. The electron microscopes can provide real-time imaging of defect nucleation and propagation. Hence, in situ electron microscopy mechanical testing is probably the most powerful in elucidating deformation mechanisms. But electron microscopes, either scanning electron microscope (SEM) or TEM, are still somewhat limited for imaging as only one electron beam (“eye”) is used.

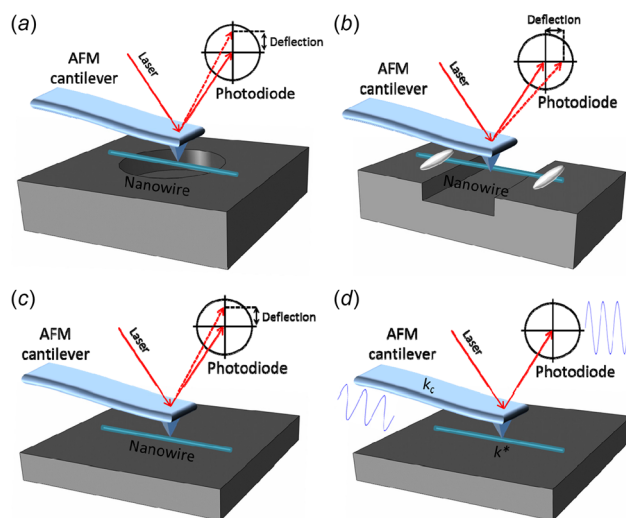


**Fig. 2** Overview of the major experimental methods for testing 1D nanostructures based on AFM: (a) contact mode, (b) lateral force mode, (c) AFM nanoindentation mode, and (d) contact resonance mode

**2.1 Atomic Force Microscopy and Nanoindenter.** AFM can be operated in mainly four modes for mechanical characterization of 1D nanostructures—(normal) contact mode, lateral force mode, nanoindentation mode, and contact resonance mode. Figure 2 shows the schematics of the four modes. Mechanical properties are extracted from the AFM data based on (1) the continuum beam bending theory (contact and lateral force modes) and (2) the elastic contact theory (AFM nanoindentation mode and contact resonance mode). For an AFM, the cantilever deflection can be measured with a resolution of 0.02 nm, thus the force resolution can reach 0.2 nN (for a typical cantilever stiffness of 10 N/m). The load resolution of a nanoindenter is circa 72 nN, and the position of the tip can be determined with a resolution of  $\sim 0.1 \text{ nm}$  [57,58].

**2.1.1 Contact Mode.** In the contact mode, samples are dispersed randomly over perforation patterns on a substrate; commonly used substrates include anodic aluminum oxide membrane

[38], rectangular silicon gratings for AFM scanner calibration (e.g., TGZ-04 from MikroMasch) [59], or patterns fabricated by FIB or microfabrication [60]. In this mode, AFM is used to deflect vertically a suspended sample to obtain the load–deflection signature. Upon contact with the sample, the AFM cantilever deflects up; the cantilever deflection is monitored using a four-quadrant photodiode, which gives rise to the applied load if the cantilever stiffness is known. The sample deflection is equal to the difference between the movement of the piezo-actuator (or substrate for some AFMs) and the cantilever deflection. With the load–deflection curve measured, elasticity theory (e.g., Euler–Bernoulli beam theory) can be used to extract the Young’s modulus and the yield or fracture strength of the NW.

More specifically, the contact mode can be implemented in two ways: (1) the deflection at a particular position as a function of the applied force and (2) the deflection profile of the entire NW by scanning the AFM tip along its length at a constant force. For a cantilevered beam and a double-clamped beam, the deflection at the loading point is given by

$$d(F, x) = \frac{Fx^3}{3EI} \quad (1a)$$

$$d(F, x) = \frac{Fx^3(L-x)^3}{3EI^3} \quad (1b)$$

respectively, where  $x$  is the distance from the fixed end,  $F$  is the applied force,  $E$  is the Young’s modulus,  $I$  is the moment of inertia, and  $L$  is the NW length. As an example, Fig. 3(a) shows the deflection measurements on a cantilevered NW following the first way. The cantilever deflection as a function of the vertical piezo-position, at several different positions along the NW length, is plotted in Fig. 3(a) (top). Curve A is obtained when applying the AFM tip directly on the substrate as a reference with the known slope of one, i.e., the cantilever deflection is equal to the movement of the piezo-actuator. With the known cantilever stiffness, the applied force versus the NW deflection is obtained, as shown in Fig. 3(a) (bottom). The slope of the linear fit yields the stiffness of the NW,  $k(x) = 3EI/x^3$ . Using this approach, one can check the consistency of the Young’s modulus measured at different locations and verify the single-clamped or double-clamped boundary condition.

To obtain the NW deflection profile  $d(x)$  following the second way, an image of the NW is acquired under a given nonzero set-point force. The NW deflection profile is then extracted from a cross-sectional cut of the image along the NW length. Figure 3(b) shows the deflection profiles of a cantilever NW and a double-clamped NW. In case that the NW might be initially slacked, a second image is acquired under a zero set-point force, which is subtracted from the first image, leading to the desired deflection profile.

Note that in the example shown in Fig. 3, the NWs were horizontally grown between two facing Si (111) sidewalls of prefabricated microtrenches, resulting in the ideal single-clamped or double-clamped boundary condition for the NWs [43]. However, typically the NWs are dispersed on top of perforation patterns, relying on only van der Waals interaction between the NWs and the substrate, which might cause ambiguous boundary conditions. Even clamping of the NWs by electron beam induced deposition (EBID) of platinum or carbon materials cannot ensure ideal boundary conditions [61,62]. In Sec. 2.4.3, discussions on how to treat such boundary conditions will be given. Another issue in the contact mode is the slippage of the AFM tip off the tested specimen. To mitigate this effect, FIB milling has been used to produce a toothlike groove that can secure the AFM tip on the NW during the scanning [63]. It is also possible that the AFM tip might slip along the NW especially at large bending of the NW. The contact mode has been widely used for testing mechanical properties of CNTs [38], and later for a variety of NWs such as Si, Ag, ZnO, LaB<sub>6</sub>, and amorphous SiO<sub>2</sub> [43,60,63–65]. In addition to bottom-up synthesized NWs, AFM has been used to test mechanical properties of top-down fabricated NWs [43].

**2.1.2 Lateral Force Mode.** In the lateral force mode, two ways of sample preparation have been used. In the first way, samples are randomly dispersed on a substrate and some of them are pinned by microfabricated islands at one end [66]. Then, AFM is used to bend the free end of a cantilevered nanostructure laterally. In this method, it is difficult to eliminate the friction force from the substrate. In the second way, samples are suspended over an FIB-fabricated trench [42]. After a desirable sample across the trench is found, electron beam induced deposition (EBID) of hydrocarbon or platinum can be used to clamp it. It is also possible to prepare suspended samples by etching a trench under a selected sample following the random dispersion [39].

In this mode, the load–deflection signature and hence the Young’s modulus and strength of the sample are obtained similar to the contact mode, with the lateral force instead of the vertical contact force. Figure 4 shows the force–displacement curves during a sequence of repeated loading and unloading cycles of a Au

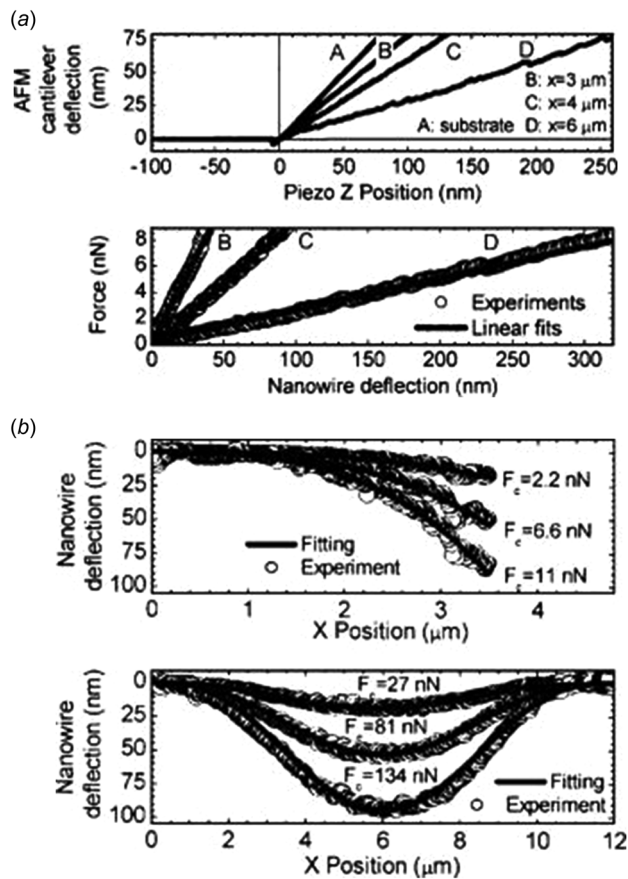


**Fig. 3 AFM contact mode.** (a) (Top) AFM cantilever deflection versus piezo-actuator position and (bottom) NW deflection at a fixed position along the NW length as a function of the applied force. Note that the NW deflection equals the piezo-actuator displacement subtracted by the AFM cantilever deflection. In the case of AFM tip directly on top of the substrate (line A), the piezo-actuator displacement equals the AFM cantilever deflection, neglecting the indentation into the substrate. (b) Deflection profile along the NW length at a constant applied force for a cantilever NW (top) and a double-clamped NW (bottom). (Reprinted with permission from Paulo et al. [43]. Copyright 2005 by American Institute of Physics).

NW. Before the mechanical testing, a tapping-mode image of the suspended NW sample was recorded. The first two curves show that the NW was elastically loaded as seen from the linear slope and reversible loading and unloading. Increased loading leads to plastic deformation in the NW. The third and fourth curves showed the same initial linear region followed by a clear turning point corresponding to the yielding. Both the elastic and plastic deformations were confirmed by subsequent AFM images of the NW sample [42].

Typically, the contact mode has better displacement (and force) resolution than the lateral force mode, but slippage of the AFM tip off the NW sample is less likely a problem for the lateral force mode. In the lateral force mode, the AFM tip moves along the centerline orthogonal to the NW sample to prevent possible slippage along the NW. The lateral force mode has been used to test mechanical properties of CNTs and SiC NWs [66], Au NWs [42], Si NWs [67], ZnO NWs [68], and Ge NWs [69].

**2.1.3 AFM Nanoindentation Mode.** According to the Hertz contact theory, the applied force  $F$  is related to the indentation displacement  $d$  by

$$F = \frac{4}{3} E^* R^{1/2} d^{3/2} \quad (2)$$

where  $E^*$  is the reduced Young's modulus  $E^* = [(1 - \nu_1)/E_1 + (1 - \nu_2)/E_2]^{-1}$  with  $E_i$  and  $\nu_i$  as the Young's modulus and Poisson's ratio for the AFM tip ( $i = 1$ ) or the NW ( $i = 2$ ), respectively, and  $R$  is the AFM tip radius.  $F$  and  $d$  in the AFM nanoindentation mode can be measured similar to those in the contact mode. Hence, the reduced Young's modulus can be measured, giving rise to the Young's modulus of the NW (assuming the Young's modulus of the AFM tip is known). The contact stiffness is given by

$$k = \frac{\partial F}{\partial d} = (6E^*2RF)^{1/3} \quad (3)$$

which is often times used to analyze the  $F$ - $d$  curve and extract the Young's modulus of the NW. Note that in Ref. [44], NW stiffness

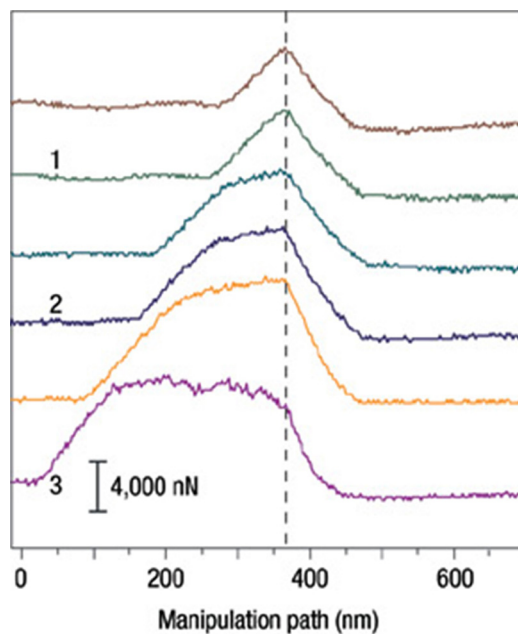


**Fig. 4 AFM lateral force mode. Force-displacement curves during a sequence of repeated loading and unloading cycles of a Au NW. (Reprinted with permission from Wu et al. [42]. Copyright 2005 by Nature Publishing Group).**

$k_{NW}$  was used in Eq. (3), which should be contact stiffness as it involves both the sample and the AFM tip. This method is easy to implement but the analysis is based on several assumptions: (1) The Hertz contact theory is assumed, which is applicable to elastic half space and might not be valid for NWs especially thin NWs; (2) The substrate is assumed to be much more rigid than the NWs, which might not be true for stiff NWs; (3) The radius of the AFM tip is assumed to be spherical; and (4) The NWs are assumed to be isotropic [44]. In the AFM nanoindentation, the force-indentation displacement curve can be converted to an indentation stress-strain curve, from which the plastic behavior can be evaluated [70].

**2.1.4 Contact Resonance Mode.** In the contact resonance mode, the elastic modulus of a sample can be extracted from the change in the resonant frequency of an AFM cantilever as a result of the sample-cantilever interaction [71-74]. Free vibration of an AFM cantilever (Euler-Bernoulli beam) can be described by the dynamic beam equation (i.e., Euler-Lagrange equation)

$$EI \frac{\partial^4 y}{\partial x^4} + \rho A \frac{\partial^2 y}{\partial t^2} = 0 \quad (4)$$

with the boundary conditions

$$y = 0, \quad \frac{\partial y}{\partial x} = 0, \quad \text{at } x = 0$$

$$\frac{\partial^2 y}{\partial x^2} = 0, \quad \frac{\partial^3 y}{\partial x^3} = 0, \quad \text{at } x = L$$

In the above equations,  $E$ ,  $I$ ,  $\rho$ , and  $A$  are the Young's modulus, moment of inertia, mass density, and cross-sectional area of the AFM cantilever, respectively. Solving Eq. (4) with the boundary conditions yields a series of resonance frequencies. When the AFM cantilever is in contact with a sample with the contact stiffness  $k$ , the second boundary condition at  $x = L$  changes to  $\partial^3 y / \partial x^3 = ky / EI$  [71]. Now solving Eq. (4) gives rise to a modified series of resonance frequencies, which depend on the contact stiffness  $k$ .

Contact stiffness following the Hertz contact model is also used in this mode, i.e., Eq. (3), as in the AFM nanoindentation mode. Hence, the Young's modulus of the sample can be obtained from the shift of the resonance frequencies. Note that sometimes Eq. (4) includes a damping term, solving which can provide the damping or dissipative property of the contact based on measurement of the vibration amplitude [74].

**2.1.5 Other AFM-Based Methods.** AFM can be used to directly pull 1D nanostructures or biomolecules, in the so-called force spectroscopy mode. In this mode, the specimen is attached between the AFM tip and a substrate. This technique was used to measure the quantized plastic deformation of gold NWs [75]. Both the AFM tip and the substrate were coated with a thin layer of gold. An atomic chain of gold (or gold NW) was formed when the AFM tip was pressed against the substrate and then pulled out. A piezopositioner was used to move the substrate and pull the NW in tension. The force and NW elongation were measured, similar to the force and NW deflection measured in the contact mode. This method has been used in measuring the mechanical properties of single biomolecules and proteins [76,77].

AFM probe has also been used to directly bend or break NWs lying on a substrate under an optical microscope [78-80]. A bent NW can be used to study the friction and shear strength at the NW-substrate interface and electromechanical coupling in the NW. Here, the AFM is used as an actuator (or manipulator) only. Indeed, a micro- or nanomanipulator can be used instead of an AFM to bend NWs [81].

**2.1.6 Nanoindentation.** Nanoindentation is a widely used method to characterize mechanical properties of bulk materials and thin films [18] and has enabled some early mechanical characterization of NWs, nanobelts, and other nanostructures [40,82–84]. A nanoindentation test of NWs using a nanoindenter is similar to the AFM nanoindentation test but different in the force range and related analyses. Note that in this paper by default nanoindentation is meant for nanoindentation using a nanoindenter, to differentiate from AFM nanoindentation. The applied force in the AFM nanoindentation is much smaller such that the NW sample undergoes only the elastic deformation. As a result, the Hertz contact theory is used in the AFM nanoindentation to extract the Young's modulus of an NW sample. But in the nanoindentation test, the NW sample likely undergoes plasticity. Then, the commonly used Oliver–Pharr model is used to extract the Young's modulus and hardness of an NW sample. However, since the indentation of an NW differs significantly from that of a half space in terms of geometry, the Oliver–Pharr model may not be readily applicable [85]. Using finite-element simulation, Shu et al. found that the Young's modulus and hardness from nanoindentation of an NW using the Oliver–Pharr model without corrections may be significantly underestimated [86]. Also because the applied force is relatively large and the NWs are typically thin, the substrate effect might need to be considered [87].

**2.1.7 Summary.** Table 1 summarizes the main AFM-based testing methods. For both the contact and lateral force modes, the samples are typically dispersed over a hole or trench and sometimes clamped by EBID especially for the lateral force mode. In both cases, the simple beam theory is used to extract the mechanical properties including Young's modulus, yield strength, and fracture strength. For the double-clamped samples, the simple beam theory should be corrected to take into account the axial tension along the samples especially under large strain [88]. In the contact mode, eccentric force might be applied on the NW sample, leading to slippage of the AFM tip off the NW, while in the lateral force mode, the lateral force calibration is more challenging than in the contact mode [89–91]. In both modes, the AFM tip might slip along the NW sample especially under large deformation.

For the AFM nanoindentation and contact resonance modes, the samples are simply dispersed on a rigid substrate. In both cases, only Young's modulus can be measured and the data reduction is based on a number of assumptions. For example, the Hertz contact theory is used, which might not apply to the tip–NW contact configuration; in addition, the substrate effect is typically neglected. Also, the AFM tip might slip off the NW sample. Of note is that Si NWs were tested using both the AFM contact mode and the AFM nanoindentation mode. It was found that the contact mode provided more accurate measurement of the mechanical properties [88].

For the force spectroscopy mode, the sample is loaded in tension, and thus, the data reduction is simple. However, this method is not widely used, likely due to the challenge in creating stable contacts between the bottom-up synthesized NWs and the AFM tip or the substrate.

For the nanoindentation by a nanoindenter, the sample preparation is the same as the AFM nanoindentation, but the Oliver–Pharr model is used instead of the Hertz contact model. Both Young's modulus and hardness can be measured, which however can be both underestimated using the Oliver–Pharr model [86]. Also, the substrate could influence the measured mechanical properties.

**2.2 Electron Microscopy.** The major advantage of performing nanomechanical testing inside an electron microscope is the in situ imaging capability. SEM imaging can record the specimen deformation (strain), fracture morphology, and some evidence of plasticity (e.g., shear band), while TEM imaging is more powerful in observing the defect dynamics. A number of testing methods have been developed for mechanical characterization of

crystalline NWs inside electron microscopes including bending [92–94] and buckling [95–97], tension [47,51,52,95,98,99], and vibration/resonance [45,46,50,61]. Most of these methods can trace back to some methods based on AFM or nanoindenter, but with external actuator and load sensor.

**2.2.1 Bending and Buckling.** Few quantitative bending tests of 1D nanostructures have been reported inside SEM or TEM, which might be because AFM-based bending tests are quite popular. Desai and Haque used a tipless AFM cantilever to bend ZnO NWs [100]. Deflections of the NW and the AFM cantilever were measured simultaneously using the SEM. Adhesion and friction forces were measured in this study. The Young's moduli of the ZnO NWs can be calculated too. Cheng et al. used a MEMS device to bend individual ZnO and Si NWs [101]. They did not investigate the elastic and fracture properties of the ZnO NWs. Instead, they investigated the anelasticity (i.e., time-dependent recovery) during the unloading. Figure 5(a) shows bending test of a ZnO NW in SEM.

Due to the large ratio of length over diameter, an NW typically buckles under compression. The buckling method has been used to measure Young's moduli of several NWs such as ZnO [95], Si [97], and Boron [96]. Buckling is essentially bending, but is simpler to implement for 1D nanostructures. Similar to the tension test, the setup for the buckling test includes an actuator and a load sensor, with the load sensor much more compliant than that used in the tensile test. Figure 5(b) shows buckling test of a ZnO NW in SEM, and Fig. 6(a) shows the force–displacement curve.

**2.2.2 Tension.** Tensile testing is the most straightforward among all the mechanical testing methods [103]. In situ TEM tensile testing of top-down fabricated microscale samples (e.g., using focused ion beam) have been recently reported [104–106]. However, top-down fabrication of feature sizes of 100 nm or below is challenging, hence for tensile testing most tested nanostructures are bottom-up synthesized. A major challenge in testing such nanostructures is nanomanipulation and high-resolution measurement of force and displacement.

Similar to the method to create thin NWs in the AFM force spectroscopy, thin metal NWs were formed with stable contacts between a metal rod and a scanning tunneling microscope (STM) probe inside TEM, especially under applied voltage [107,108]. Stable contacts can also form between thin metal NWs inside TEM by cold welding [109].

Ruoff and coworkers reported the first tensile testing of individual CNTs inside SEM [47]. Two AFM cantilevers were used in the test with a stiff and a compliant cantilever used as the actuator and the load sensor, respectively. EBID of hydrocarbon was used to create stable contacts between an individual CNT and two AFM tips. This work could be viewed as extending the AFM force spectroscopy into SEM [75].

The stiff AFM cantilever (actuator) used in Ruoff's work can be replaced with an even stiffer and sharp tungsten probe, which, when attached to a nanomanipulator, can be directly used to manipulate 1D nanostructures. Zhu et al. used such a tungsten probe for manipulating and conducting tensile testing of Si NWs in SEM, with a compliant AFM cantilever as the load sensor [51]. Assuming SEM resolution of 1 nm, strain resolution of 0.03% can be obtained for an NW of 3  $\mu\text{m}$  in length. For an AFM cantilever (load sensor) with stiffness of 1 N/m, the load resolution of 1 nN is obtained, leading to stress resolution on the order of 1 MPa for a typical NW with diameter <100 nm. Subpixel resolution can be obtained using digital image correlation (DIC), resulting in better strain and stress resolutions [110]. Figure 5(c) shows tension test of a Si NW in SEM, and Fig. 6(b) shows the stress–strain curve. However, the compliant AFM cantilever (load sensor) could rotate especially under high force, introducing a bending component into the tensile loading condition.

A double-clamped, microfabricated flexure beam has also been used as the load sensor, which can eliminate the end rotation

problem of the AFM cantilever. Using this load sensor and a nanomanipulator probe, tensile tests of Cu [52] and Ag NWs were performed.

**2.2.3 Vibration/Resonance.** Resonance is a simple yet widely used method to measure Young's modulus of 1D nanostructures. According to a simple beam theory, the  $n$ th mode resonance frequency of a cantilevered beam is given by

$$\omega_n = \frac{\beta_n^2}{L^2} \sqrt{\frac{EI}{\rho A}} \quad (5)$$

where  $E$  is the Young's modulus,  $I$  is the moment of inertia,  $L$  is the beam length,  $A$  is the cross-sectional area, and  $\rho$  is the beam density. The  $\beta_n$  term is the eigenvalue from a characteristic equation in Ref. [111]. When the resonance frequency is measured, the Young's modulus can be calculated according to Eq. (5).

The resonance can be excited by thermal [45], electrostatic [46,50], or mechanical [48,61] means. Figure 5(d) shows resonance test of a ZnO NW in SEM excited by mechanical vibration, and Fig. 6(c) shows the resonance peak from which the resonance frequency can be determined. The NWs can be directly grown on a substrate or clamped onto a probe using EBID. NWs attached to a substrate by van der Waals force only have been tested using the resonance method, which however might lead to underestimation of the Young's modulus [61]. It is important to distinguish so-called forced resonance and parametric resonance. Assuming the fundamental natural frequency  $\omega_0$ , forced resonance occurs at driving frequency  $\omega = \omega_0$ , while parametric instability occurs at  $\omega = 2\omega_0/n$  ( $n$  integer not smaller than 1). More details on the parametric resonance can be found elsewhere [50,112].

**2.3 MEMS-Based Testing Methods.** It is worth discussing MEMS-based mechanical testing methods in a separate section. MEMS consist of micrometer-scale components but offer nanometer displacement and nano-Newton force resolutions. MEMS have been widely used in mechanical testing of thin films [113–116]. They can also be used for nanomechanical characterization by controlled actuation with high precision and high speed, high-resolution force/displacement measurements, and integrated multifunctions. In addition, their tiny size makes them ideal for in situ SEM/TEM testing. There has been extensive interest in the past decade in developing MEMS-based stage for in situ SEM/TEM testing of nanostructures [49]. More details on MEMS-based nanomechanical testing have been reviewed elsewhere [117,118]. In this review, only a brief summary of the major advances in this area will be given.

Haque and Saif reported a MEMS stage to characterize nano-scale thin films that are cofabricated with the stage inside SEM and TEM [129,136,167]. The stage was actuated by an external piezo-actuator with a mechanism that can mitigate misalignment. Zhu and Espinosa have developed the first MEMS stage that includes an on-chip actuator and an electronic load sensor with a gap in between [49,121–123]. Two types of MEMS actuators were used: thermal actuator for displacement control and comb-drive actuator for force control; the electronic load sensor was based on differential capacitive sensing. The main novelty of their work was the introduction of an electronic load sensor; displacement of the load sensor was measured electronically instead of commonly used microscope imaging. Figure 7(a) shows the MEMS stage with the thermal actuator and the capacitive load sensor. A number of similar MEMS stages have been developed thereafter for testing a wide variety of 1D nanostructures [125–132].

MEMS testing stages consisting of two separated capacitive sensors to record both the specimen displacement and load have been developed [123,124,133]. In this case, specimen elongation was also measured electronically (instead of microscope imaging) in addition to load sensor displacement. As a result, such stages

are uniquely suited for fatigue tests in situ or ex situ; Fig. 7(b) shows one such stage. Fatigue test of Au ultrathin films (nanobeams) has been conducted using this stage [124].

It is of relevance to characterize the thermomechanical behavior of 1D nanostructures for their device applications. Chang and Zhu recently developed an MEMS thermomechanical stage with an on-chip heater that can heat from room temperature up to 600 K [54]. The MEMS stage consists of a comb-drive actuator, a capacitive load sensor, and a heater based on Joule heating next to the specimen area, as shown in Fig. 7(c). The entire stage is symmetric to ensure that the temperatures on both sides of the specimen are equal so as to prevent temperature gradient and heat flow through the specimen. Note that the capacitive sensor is also in

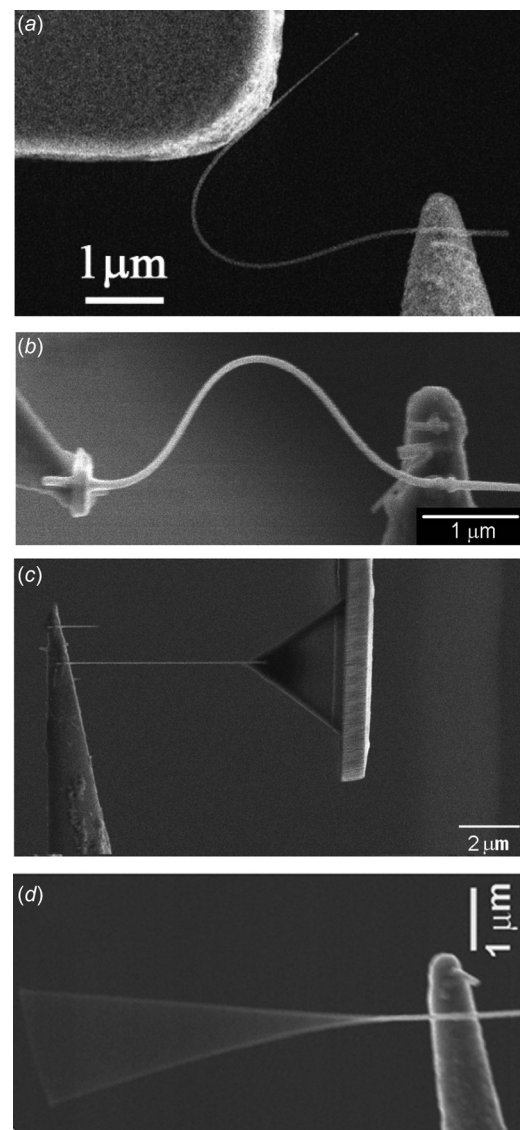


**Fig. 5** (a) Bending test. An NW clamped on a nanomanipulator probe is bent in an MEMS device. (Reprinted with permission from Cheng et al. [101]. Copyright 2015 by Nature Publishing Group.) (b) Buckling test. An NW is compressed to buckling between a nanomanipulator probe (actuator) and an AFM cantilever (load sensor) (from Ref. [53]). (c) Tension test. An NW is pulled between a nanomanipulator probe (actuator) and an AFM cantilever (load sensor). (Reprinted with permission from Zhu et al. [51]. Copyright 2009 by American Chemical Society.) (d) Resonance test. An NW clamped on a nanomanipulator probe is excited to resonance by mechanical vibration. (Reproduced with permission from Qin et al. [61]. Copyright 2012 by Wiley).

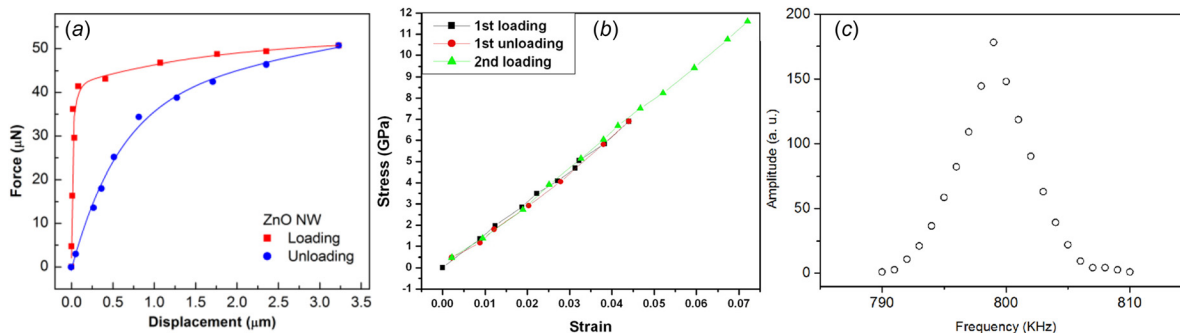


**Fig. 6** (a) Force–displacement curve in a buckling test. (Reprinted with permission from Cheng et al. [101]. Copyright 2015 by Nature Publishing Group.) (b) Stress–strain curve in a tension test. (Reprinted with permission from Zhu et al. [51]. Copyright 2009 by American Chemical Society.) (c) Amplitude–frequency curve showing a resonance peak in a resonance test. (Reprinted with permission from Chang et al. [102]. Copyright 2016 by Elsevier.)

the form of comb drive, identical in geometry to the comb-drive actuator. Chen et al. achieved temperature control for mechanical testing of NWs by placing their MEMS stage inside a vacuum cryostat including a heater, a cooling channel with liquid nitrogen circulation, and a temperature controller [134]. Kang and Saif fabricated a novel MEMS stage for in situ uniaxial testing at high temperatures [135]. The stage was fabricated out of SiC, which can sustain temperature up to 700 °C, much higher than those made of Si.

It is of relevance to investigate the multiphysical coupling of nanostructures, especially how mechanical strain can tune other physical properties—so-called elastic strain engineering. Bernal et al. developed an MEMS stage to characterize electromechanical coupling of NWs, combining four-point electric measurement and tensile loading [136]. Zhang et al. [132] fabricated an electromechanical MEMS stage with a SiO<sub>2</sub> layer beneath the structural layer for insulation. Murphy et al. reported thermal conductivity of Si NWs as a function of tensile strain [137]. While the MEMS

stage was used to apply tensile strain to the specimen, Raman spectroscopy was used to measure its thermal conductivity. Of note is that most MEMS-based in situ testing has been performed inside SEM or TEM. Integration of MEMS stages with spectroscopy such as Raman and photoluminescence (PL) could offer exciting new opportunities for mechanical testing of nanostructures especially multiphysical testing.

**2.4 Experimental Issues.** Several commonly encountered experimental issues are discussed here. Specific ones such as potential sample heating in MEMS testing stages using thermal actuators [138] are not included.

**2.4.1 Sample Preparation.** A key but challenging step in nanomechanical testing is to manipulate and position specimens with nanometer resolution and high throughput. For tensile testing, this step becomes even more challenging as the specimens must be freestanding, aligned with the loading direction and

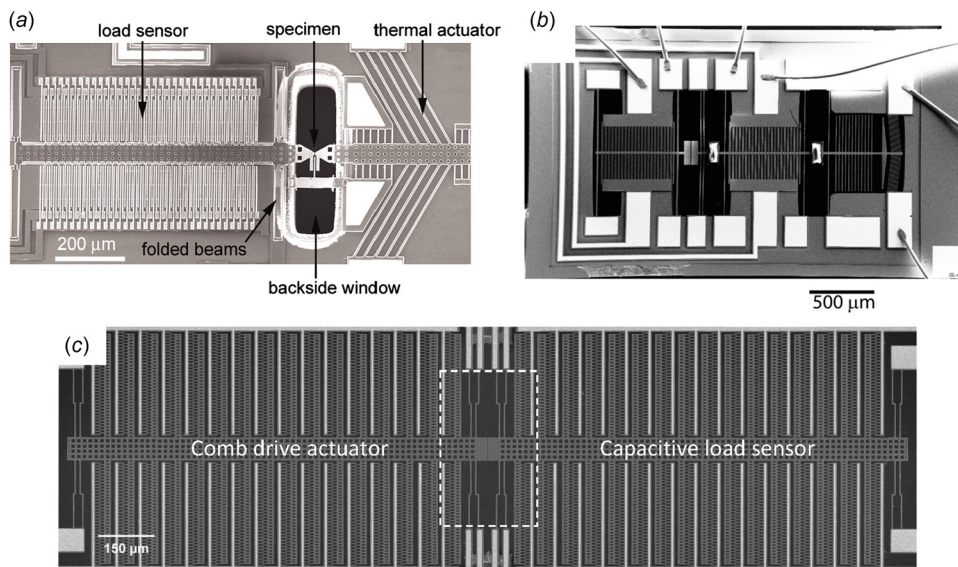


**Fig. 7** (a) An integrated MEMS testing stage for mechanical testing of single NWs (from Ref. [49]). The stage includes a thermal actuator and a capacitive load sensor with a gap in between, across which the NW sample is mounted. (b) A MEMS stage for fatigue testing. (Reprinted with permission from Hosseini and Pierron [124]. Copyright 2013 by Royal Society of Chemistry.) Compared to the one in (a), one more capacitive sensor is included to measure sample displacement digitally. (c) A MEMS stage including an on-chip heater based on Joule heating (the boxed region in the center). (Reprinted with permission from Chang and Zhu [54]. Copyright 2013 by American Institute of Physics.) This stage features a symmetric actuator and load sensor design to ensure the same temperature at both ends of the sample.

clamped at both ends. Methods for manipulation and positioning of 1D nanostructures include “pick-and-place” by a nanomanipulator [49] and dielectrophoresis [131,139] in addition to cofabrication and direct synthesis. EBID of amorphous carbon or platinum is commonly used to clamp the nanostructures. However, recent studies showed that such clamps have certain compliance and could affect the measured mechanical properties [61,62]; see Sec. 2.4.3 for more details. To alleviate this issue, displacement markers can be deposited on the NW for local displacement measurement [55,62,140]. Adhesives (e.g., epoxy) have also been used to clamp nanostructures like polymer nanofibers [141], CNTs [142], and Ni nanobeams [124]. However, in this case individual samples can only be manipulated under an optical microscope, which might limit this method to relatively large sample size. Also, compliance of the adhesives is of potential concern. More details on the sample preparation can be found elsewhere [57,118,143].

**2.4.2 Vertically Aligned NWs.** For all the experimental methods discussed so far, individual NW samples are either mounted in a freestanding manner or dispersed on a substrate, which require some sample preparation. However, it is quite common that as-synthesized crystalline NWs especially semiconductor and metal NWs are vertically aligned on a substrate. Hence directly measuring the mechanical properties of such as-synthesized NWs would be of great interest to eliminate sample preparation and avoid ambiguous boundary condition. The AFM lateral force mode was used to deflect the vertically aligned ZnO NWs and measure the Young’s modulus of individual ZnO NWs [144]. In another case, the substrate with vertically aligned Si NWs was cleaved to expose an array of cantilevered NWs at the cleaved edge. Then, AFM was used to deflect multiple locations along the NW length in the contact mode [145]. As-synthesized ZnO NWs were also excited to resonance by an electrostatic field [50].

Some vertically aligned NWs are grown on a substrate by epitaxy. These NWs strongly bond to the substrate. Bending tests have been used to measure their fracture strengths [93]. In the bending test, an AFM cantilever attached to a nanomanipulator system was used to deflect an NW in the lateral direction. This method was used to measure the bending strength of [111]-oriented Si NWs synthesized by the popular vapor–liquid–solid (VLS) method. Using a rigid nanomanipulator tip instead of the AFM cantilever, Chen and Zhu measured the fracture strain of ZnO NWs under bending [92].

**2.4.3 Effect of Boundary Condition.** One challenge for AFM contact mode or lateral force mode is the uncertainty of the boundary conditions, which can range from simply supported to doubly clamped. For NWs without EBID-based clamps, the exact boundary condition depends on adhesion between the sample and the substrate and relative stiffness of the sample and the substrate. To overcome this challenge, one method is to probe at multiple locations along the sample length. Therefore, the deflection profile can be obtained instead of isolated midpoint bending measurement. For NWs with small diameters, the deflection profiles were fitted best with doubly clamped boundary condition, while for NWs with large diameters, the deflection profiles were fitted better with simply supported boundary condition [59] (Fig. 8(a)).

Even in the case of EBID-based clamping, the clamps are still relatively compliant. It has been found necessary to investigate the effect of the clamping on the measured mechanical properties. Using the resonance test, Xu and coworkers studied the effect of clamping on the measured Young’s modulus of ZnO NWs [61]. The NWs were clamped on a tungsten probe in the configuration of a cantilever by EBID of hydrocarbon for in situ SEM resonance tests. EBID was repeated several times to deposit more hydrocarbons at the same location. The resonance frequency was found to increase with the increasing clamp size until approaching that under the “fixed” boundary condition (Fig. 8(b)). The critical clamp size was fitted into a function of NW diameter and NW

Young’s modulus, which can provide valuable guidance for testing other NWs using EBID-based clamping.

Gianola and coworkers reported that the stiffness of the EBID clamps commonly used for nanomechanical testing is comparable to that of inorganic NWs [62]. As a result, significant errors can be introduced in measurements of displacement, and hence strain and Young’s modulus; the extent of the errors would depend on the stiffness of the sample and the geometry of the clamp. In addition, the clamps can be deformed permanently, which might be misinterpreted as plastic deformation in the NWs.

**2.4.4 Effect of Loading Mode.** The elasticity size effect can be generally attributed to two mechanisms [37]: surface elasticity [146–150] and bulk nonlinear elasticity (as a result of the surface stress) [151]. Under different loading modes, the elasticity size effect manifests differently for different mechanisms [53,146,152]. For instance, in the case of surface elasticity, the elasticity size effect would be stronger under bending than under tension as the surface plays a more important role under bending. More specifically, the NW Young’s modulus  $E = E_c + 8(S/D)$  and  $E = E_c + 4(S/D)$ , respectively, under bending and tension, where  $E_c$  is the Young’s modulus of the core and  $D$  is the NW diameter [53]. Therefore, for probing the underlying mechanism of the elasticity size effect, it is of relevance to measure the Young’s moduli under different loading modes. Zhu and coworkers measured the elasticity size effect of ZnO NWs under both tension and buckling [53] (Fig. 9); the buckling test should give rise to the Young’s modulus under bending. However, in the bulking test the measured Young’s modulus sensitively depends on the NW diameter (fourth power in contrast to square in the case of tension), thus the buckling method could lead to larger error in measuring the Young’s modulus [112]. Resonance test can be a more accurate method to measure the Young’s modulus under bending. Recently, the same group measured the Young’s modulus of the same Ag NW using the resonance test followed by the tensile test. After the resonance test, the same NW was transferred to an MEMS stage for the tensile test [102].

### 3 Mechanical Properties of Crystalline Nanowires

Crystalline NWs exhibit considerably different mechanical behaviors from their bulk counterparts as a result of large surface-to-volume ratio. Free surfaces can lead to many interesting properties such as size-dependent elasticity [37,149,151], size-dependent yield strength [153], and surface dislocation nucleation [32–34], to name a few.

**3.1 Elasticity.** It would be illustrative to think that the atoms on the free surfaces are created by cleaving a bulk material. As a result, the surface atoms have fewer bonding neighbors, or a lower coordination number, than do atoms in the bulk. Such a coordination number deficiency leads to surface stress and an effective Young’s modulus of surface atoms, which is different from that of bulk atoms [37].

The surface atoms can be stiffer or softer than the bulk atoms [149]. The softening effect is primarily due to the bond loss (i.e., loss of neighboring atoms on the surface). In contrast, the stiffening effect can be attributed to the electron redistribution (often called bond saturation) [149,154]. For NWs made of covalent or ionic bonds, the surfaces tend to reconstruct, forming periodic patterns. For these NWs, the surface stresses are typically compressive, which leads to an increase in NW length at equilibrium. At the same time, the surface atoms significantly contract toward the bulk, leading to overall smaller interatomic spacing and volume contraction near the surface [103,154]. For NWs of covalent bonding, the smaller interatomic spacing indicates a higher electron density (assuming bonding electrons are localized in covalent systems), which can contribute to surface stiffening [154]. For NWs of ionic bonding, the smaller interatomic spacing

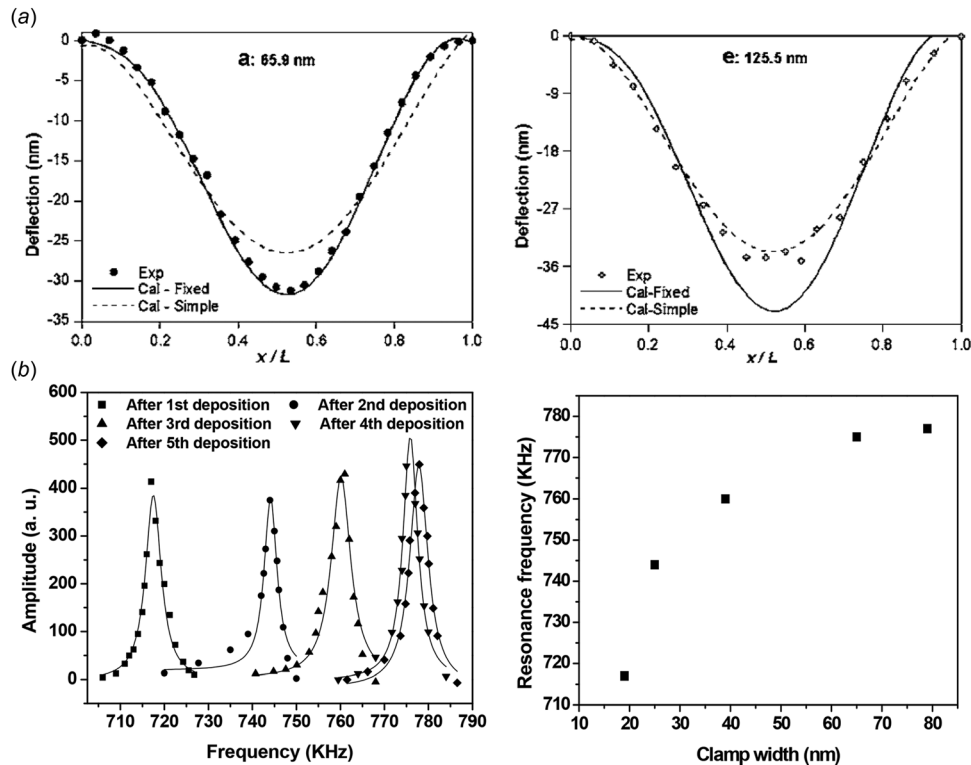


**Fig. 8** (a) The deflection profiles along the NW sample length under AFM contact mode. (Left) For an NW with diameter of 65.9 nm (small diameter), the deflection profile was fitted best with doubly clamped boundary condition; (right) for an NW with diameter of 125.5 nm (large diameter), the deflection profile was fitted better with simply supported boundary condition. (Reprinted with permission from Chen et al. [59]. Copyright 2006 American Institute of Physics.) (b) The resonance frequency as a function of the clamp size for a ZnO NW under resonance in SEM. (Left) The resonance peaks for different clamp sizes, and (right) the resonance frequency increases with the increasing clamp size. (Reproduced with permission from Qin et al. [61]. Copyright 2012 by Wiley).

additionally causes stronger (long-range) Coulomb force (electrostatic force), which can also contribute to surface stiffening [98].

The surface stress is typically tensile for FCC metals, which leads to contraction of the NW length at equilibrium. The contraction allows surface atoms to increase their coordination number and their electron density, contributing to stiffening effect. But whether a particular surface is softer or stiffer depends on the competition between bond loss and electron redistribution on the

surface [37]. In the case of Cu NWs, Zhou and Huang found that the Young's modulus along  $\langle 110 \rangle$  direction on  $\{100\}$  surface is larger than its bulk counterpart, but smaller along  $\langle 100 \rangle$  direction on  $\{100\}$  surface [149].

In addition to the aforementioned surface elasticity, there is another mechanism that contributes to the overall stiffening or softening of NWs—so-called bulk nonlinear elasticity. Liang et al. found that the axial compressive strain caused by the tensile surface stresses in metallic NWs is large enough to induce a nonlinear increase in the Young's modulus of bulk atoms. For Cu NWs along  $\langle 001 \rangle$ ,  $\langle 110 \rangle$ , and  $\langle 111 \rangle$  crystallographic directions, while the surface is always softer than an equivalently bulk, and the overall NW softening or stiffening is determined by orientation-dependent core elasticity, more specifically, increase in the  $\langle 110 \rangle$  direction but decrease in the  $\langle 001 \rangle$  and  $\langle 111 \rangle$  directions [151].

As a result of the surface stress and surface elasticity, the crystalline NWs can exhibit marked elasticity size effect, i.e., Young's modulus as a function of NW diameter. The surface stress and surface elasticity can influence the mechanical behaviors of NWs under tension, bending, buckling, and other deformation modes [155–160].

**3.1.1 Covalent Bonding.** Several types of semiconductor NWs with covalent bonding have been investigated. Here, Si NWs will be discussed as an example. Zhu et al. reported the quantitative stress-strain measurements of Si NWs using tensile testing for the first time [51]. The Si NWs were synthesized by the VLS process, and the NWs tested ranged from 15 to 60 nm in diameter. Their results showed clear size effects—the Young's modulus decreases with the decreasing diameters when the

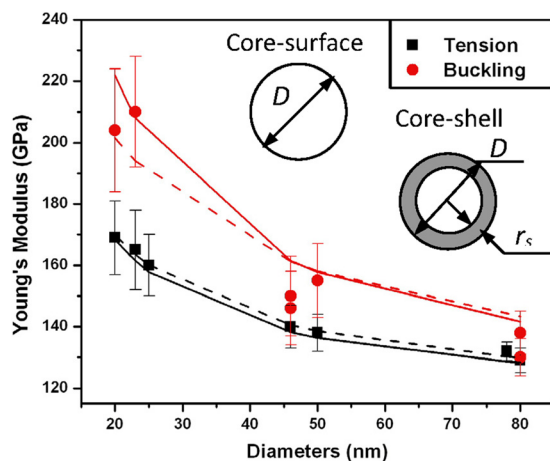


**Fig. 9** The Young's modulus of ZnO NWs as a function of the NW diameter. The stiffening size effect is more pronounced under bending (buckling) than under tension (from Ref. [53]).

diameter is below about 30 nm [51]. However, Heidelberg et al. found essentially no size effects [67], while Gordon et al. found a stiffening trend [145]. Figure 10(a) shows the available Young's modulus data of Si NWs from both experiments and simulations.

Several mechanisms have been put forth to account for size effects in elasticity of NWs including: (1) surface effects (surface stress and surface elasticity), (2) nonlinear elastic response of the NW core, and (3) increasing importance of the oxide layer. But

for the Si NWs in the work of Zhu et al., high-resolution TEM images showed that there was little or no visible amorphous oxide on the surface [51]. So, the oxide layer likely played a negligible role in the measured Young's modulus of Si NWs. Using density function theory (DFT) calculations of  $\langle 100 \rangle$  Si NWs, Lee and Rudd found that the nonlinear bulk elasticity had a negligible effect on the Young's modulus of Si NWs [161]. Thus, a possible mechanism for the elasticity size effect of Si NWs was the surface elasticity, more specifically, the softening size effect due to the bond loss [149,154]. Of note is that multiscale resonance calculations also predicted similar elastic softening in  $\langle 100 \rangle$  Si NWs in the similar diameter range [172].

**3.1.2 Ionic Bonding.** The extent of ionic character in a bond is related to the electronegativity difference of the elements in the bond. As in most group II–VI materials, the bonding in ZnO is largely ionic with certain extent of being covalent.

Chen et al. performed resonance tests to measure the Young's modulus of  $[0001]$ -oriented ZnO NWs with diameters ranging from 17 to 550 nm [50]. When the diameters of the ZnO NWs were smaller than  $\sim 120$  nm, the Young's modulus increased with the decreasing diameter (i.e., elasticity size effect). When the diameters were larger than 120 nm, the Young's modulus approached to that of bulk ZnO. Such a size effect was attributed to a surface stiffening effect as a result of bond length contraction near free surfaces, which extends several layers deep into the bulk and fades off slowly [173].

Agrawal et al. performed in situ TEM tensile tests on  $[0001]$ -oriented ZnO NWs using an MEMS testing platform [98]. A similar size effect in Young's modulus to Chen et al. was reported; more specifically, the modulus increased as the diameters decreased below  $\sim 80$  nm, while NWs with larger diameters showed a Young's modulus close to the bulk value (140 GPa). MD simulations found that the surface atoms significantly contract toward the bulk during surface reconstruction, leading to overall smaller interatomic spacing near the surface and stronger Coulomb force, which is the main cause of the stiffening size effect. Using DFT-based ab initio calculations, Zhang and Huang found that the stiffening size effect is primarily due to surface bond saturation (electron redistribution) instead of bulk nonlinear elasticity [174]; bulk nonlinear elasticity was proposed by several atomistic simulation studies [175,176]. Surface electron redistribution is known to be a common mechanism for surface elasticity in covalent materials [37,149]. Hence, Zhang and Huang's result is not surprising in view that ZnO bonding is partially covalent.

Xu et al. performed in situ SEM tests on  $[0001]$ -oriented ZnO NWs to measure their Young's modulus under both uniaxial tension and buckling [53]. The experimental setup involved a nano-manipulator probe (actuator) and an AFM cantilever (load sensor). Using the same setup, both uniaxial tension and compression (buckling) were conducted. Note when buckled, an NW is effective under bending. It has been reported that different loading modes can manifest the size dependence of the Young's modulus differently, due to the greater influence of surface elasticity under the bending mode [146]. Xu et al. found that for ZnO NWs, the Young's modulus under bending was larger than that under tension, which revealed that the surface has a higher elastic modulus [53]. This result is consistent with the previously results mentioned above that generally favor the surface elasticity effect instead of the nonlinear bulk elasticity effect. Figure 10(b) shows the available experimental data on Young's modulus of ZnO NWs.

Bernal et al. found a similar stiffening size effect in GaN NWs, though much smaller in magnitude than ZnO NWs [177]. The difference was attributed to the lower Young's modulus of ZnO; a material of lower Young's modulus can deform more by the (relaxation-induced) same level of surface stress.

**3.1.3 Metallic Bonding.** A variety of methods have been used to synthesize metallic NWs including electrochemical deposition

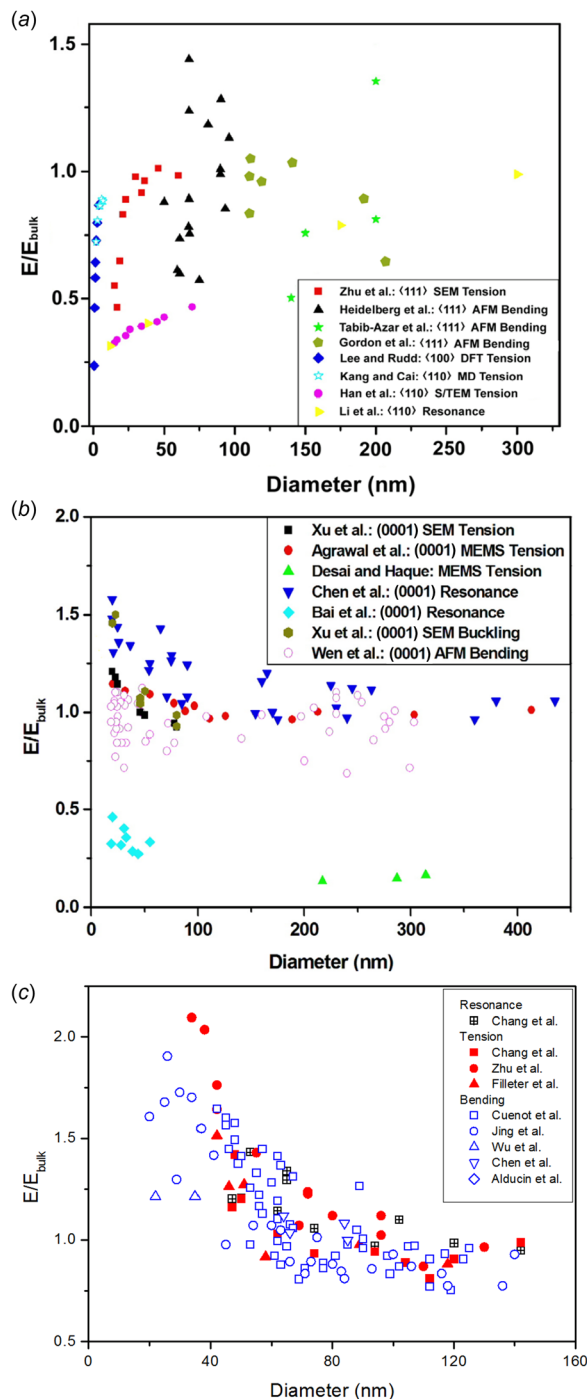


**Fig. 10** (a) Elasticity size effect of Si NWs [51,67,153,161, 162–165]. The data are normalized by the bulk value in the  $\langle 111 \rangle$  orientation. (b) Elasticity size effect of ZnO NWs [50,68,95, 98,166,167]. The data are normalized by the bulk value in the  $[0001]$  orientation. (c) Elasticity size effect of Ag NWs [41,60, 102,168–171]. The data are normalized by the bulk value in the  $\langle 110 \rangle$  orientation.

[178] and physical vapor deposition [52,179]. Among all the metallic NWs, pentatwinned (also called fivefold twinned) NWs synthesized by the polyol method in solution phase [180] are unique in microstructure—each NW has five twin segments joined along a common quintuple line in the axial direction. The synthesis method is relatively easy and scalable; as a result, most experimental studies on mechanical properties of metallic NWs are about pentatwinned metal NWs, especially Ag NWs.

Both experimental and simulation results on the Young's modulus of pentatwinned Ag NWs exhibit large discrepancies. Using in situ SEM or TEM tensile tests, Zhu et al. [168] and Filleter et al. [169] reported pronounced stiffening effect, i.e., an increase of Young's modulus with decreasing NW diameter. Using AFM bending tests, Jing et al. [60] found a similar stiffening effect. In contrast, Wu et al. [170] and Chen et al. [59] reported Young's moduli that are higher than the bulk value but without obvious size effect. In all the experiments above, the NWs were  $\langle 110 \rangle$  oriented with diameters typically between 20 and 140 nm.

Some atomistic simulations showed pronounced stiffening size effect but no apparent effect of the pentatwinned microstructure compared to the single-crystalline counterpart [181]. Other atomistic simulations revealed the similar size effect, but also showed strong effect of the pentatwinned microstructure (i.e., higher Young's modulus than that of the single-crystalline counterpart) [182,183]. The microstructure effect was attributed to the high compressive at the core of the pentatwinned NW. Similar conclusions on the size and microstructure effects were observed in other pentatwinned FCC NWs including Cu, Au, Ni, and Pd [184,185]. More recently, Bitzek and coworkers reported a systematic study on the Young's modulus of several types of FCC pentatwinned NWs [186]. The authors found that while the size effect is due to atomic origin (e.g., surface stress and surface elasticity), the effect of the pentatwinned microstructure is due to compatibility constraint imposed by the microstructure and elastic anisotropy of the FCC metal.

Under different loading modes, the elasticity size effect can manifest differently for different mechanisms, as mentioned in Sec. 2.4.4. Zhu and coworkers recently addressed the discrepancy about the size-dependent Young's modulus of pentatwinned Ag NWs [102]. Two independent experiments on the same NW, in situ SEM resonance test and tensile test, were used to measure the Young's moduli. For tension, the Young's modulus was extracted as the slope of the linear elastic regime instead of the slope during unloading because pentatwinned Ag NWs were found to exhibit recoverable plasticity and Bauschinger effect [55,187]. Zhu and coworkers also measured the cross-sectional shape of the Ag NWs as a function of the NW diameter, which was found to transit from pentagon to circle with decreasing NW diameter. The effect of the cross-sectional shape on the measured Young's modulus was evaluated. This work confirmed that the Young's modulus of pentatwinned Ag NWs increases with decreasing NW diameter, though the size effect is less pronounced compared to their previous result [168]. Figure 10(c) shows the available experimental data on Young's modulus of Ag NWs. The comparison of the measured Young's moduli under both bending and tension illustrated that some combination of core nonlinear elasticity and surface elasticity is responsible for the observed elasticity size effect in pentatwinned Ag NWs. In Ref. [168], the effect of surface elasticity on pentagonal and circular cross sections was calculated. The effect was generalized to a regular pentagonal cross section with any number sides [188].

**3.2 Fracture.** In contrast to the reported, often opposite trends in the size effect on elasticity, there is a general agreement in the literature that fracture strength of Si NWs increases with the decreasing size. Figure 11(a) shows the available fracture strength data of Si NWs as a function of NW diameter. For example, Zhu et al. found that the fracture strength increased to  $>12$  GPa as the NW diameter decreased to 15 nm or so [51]. They have further

plotted the fracture strength versus the side surface area of the Si NWs, as shown in Fig. 12(a). The mean fracture strengths from Si thin films [199] and NWs [51,88,127,189–194] are included in the same figure for comparison. For both the thin films and NWs, the fracture strength increases with the decreasing side surface area, although their fabrication methods are very different (microfabrication for thin films and VLS synthesis for NWs) [200].

Interestingly, with the decreasing side surface area, the increase rate of the fracture strength for the NWs was observed to be much higher than that for the thin films. For single-crystalline and polycrystalline Si thin films, the fracture origin is mainly attributed to the surface topography as a result of chemical etching (and sometimes thermal annealing) during microfabrication [199,201–204]. The slope difference in Fig. 12(a) suggests two possible hypotheses: (1) Si NWs synthesized by the VLS method have lower density of surface defects and thus better surface quality, compared to thin films fabricated using the etching methods, and (2) the fracture origin of VLS-synthesized Si NWs might be different from that of microfabricated Si thin films, i.e., other sources such as internal defects might contribute.

Point defects (e.g., dopant and catalyst atoms) and planar defects (e.g., stacking faults) have been reported for many VLS-synthesized semiconductor NWs. Dopants are incorporated into NWs either intentionally or unintentionally [205,206]. During VLS synthesis, dopants can be diffused into the NW core through the catalyst and onto the surface by uncatalyzed decomposition [207]. Given the higher surface doping, dopants can diffuse into the core. Planar defects such as stacking faults were found to exist inside Si NWs; interestingly, the density of stacking faults increased for smaller NWs [208].

Similar to Si NWs, ZnO NWs also display strong size effect in the fracture strength, with the NWs of smallest diameters approaching the theoretical strength ( $E/10$ – $14$  GPa) [53,68,94,195,209], see Fig. 11(b). Two mechanisms have been proposed to account for the observed size effect based on surface defects and point defects (vacancies), respectively. The first mechanism based on surface defects correlated strength with surface imperfections [195]. Weibull statistics showed that there is a correlation between surface area and fracture strength, suggesting that surface defects play an important role in NW fracture. The second mechanism correlated failure with vacancies existing inside NWs [210]. Weibull statistics showed an excellent fitting (Fig. 12(b)). In addition, in situ cathodoluminescence (CL) study indicated that vacancies might be present in the ZnO NWs. However, no direct evidence of the presence of vacancies was provided.

The fracture behavior of NWs could be due to a combination of surface defects and (internal) point defects, as discussed above in the case of Si and ZnO NWs. However, it remains challenging to quantify the specific role of each type of defects because it is difficult to identify the density and distribution of both types of defects especially the point defects. Indirect evidences, however, have suggested the presence of point defects in semiconductor NWs and their role in mechanical properties. As mentioned above, CL spectrum of ZnO NWs identified an extra peak that is likely correlated with oxygen vacancies [209]. More recently, Zhu and coworkers reported a giant anelasticity in ZnO and doped Si NWs, which was attributed to motion of point defects under an inhomogeneous strain field. Their electron energy loss spectroscopy (EELS) study confirmed the presence of point defects [101]. A direct method to identify density and distribution of point defects is atom probe tomography (APT), down to the single-atom level [211,212]. A specific technique of APT, local electrode atom probe (LEAP), has been used to identify the atomic species and their spatial distribution in a single NW [206].

Mechanical properties of SiC NWs have been measured via in situ SEM tensile tests using a MEMS platform [196], where another type of internal defects, stacking faults, was found to play a critical role. The SiC NWs, synthesized by the VLS process, had the  $\langle 111 \rangle$  growth direction [213]. The microstructure of SiC NWs consisted of pure 3C structure, 3C structure with an inclined

stacking fault, and highly defective structure in a periodic fashion along the NW length. The SiC NWs were reported to fail in brittle fracture at room temperature, in contrast to the superplasticity reported previously [214]. The SiC NWs exhibited strong size effect in the fracture strength, that is, the fracture strength increased with decreasing diameter, up to >25 GPa approaching the theoretical strength of 3C SiC. An interesting observation was that all the cracks initiated and propagated in the 3C segments with the 19.47 deg stacking faults rather than in the highly defective segments, in good agreement with MD simulations [215]. It appears that for SiC NWs, the size effect on fracture strength was due to the size-dependent defect density (of the 3C structure with 19.47 deg stacking faults), rather than the surface effect as commonly believed [196]. Figure 11(c) shows the available fracture strength data of SiC NWs as a function of NW diameter.

**3.3 Plasticity.** Following nucleation of the leading partial dislocations from free surfaces [31–33], both slip (via either perfect or partial dislocations) [32–34,216–218] and twinning [179,219,220] have been observed in metallic NWs. The

competition between these deformation mechanisms is influenced by loading type, NW diameter, NW orientation, side surface orientation, and temperature, which can be rationalized by Schmid factors of the leading and trailing partial dislocations and generalized stacking fault energies [36]. Figures 11(d) and 11(e) show the fracture strengths of Ag and Cu NWs, respectively. Here fracture strength refers to failure strength under different loading modes. Note that in some cases yield strength or flow stress data were included; in some metal NWs yield strength is close to failure strength as a result of limited plasticity.

Slip by partial dislocations has been reported in single-crystalline Pd NWs [218] and pentatwinned Ag NWs [197]. Figure 13(a) shows the stress–strain curve of a Pd NW and the TEM image of the fracture surface of the Pd NW. The stress–strain curve exhibited a nonlinear elastic relationship before an abrupt fracture at ~6 GPa. The TEM image showed the shear fracture with a shear plane of {111} and a number of stacking faults parallel to the major shear plane (and the equivalent shear plane). It was hypothesized that the shear fracture occurred by activation of a series of identical partial dislocations from the free surfaces. For a <110>-oriented Ag NW, postmortem TEM image displayed two

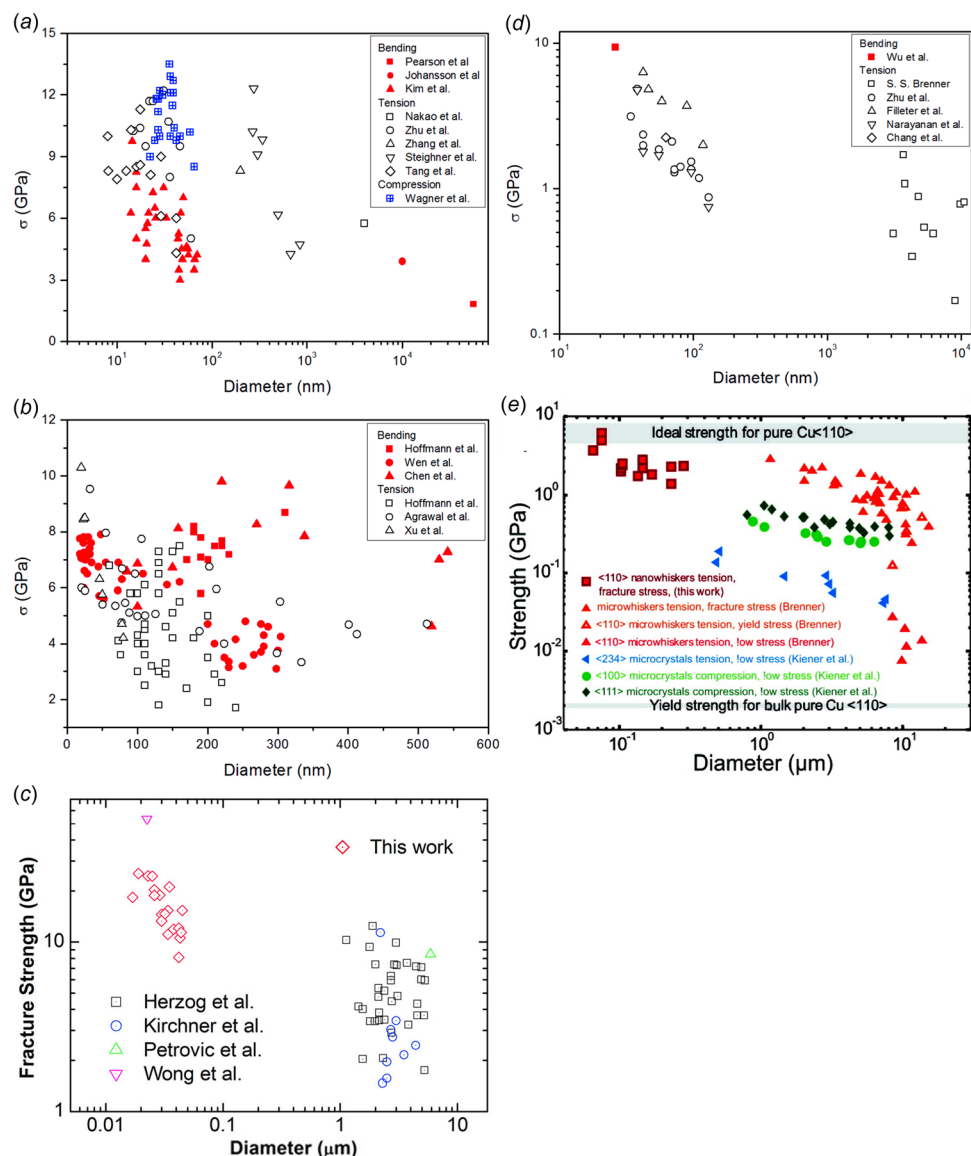


Fig. 11 Fracture strength as a function of NW diameter for (a) Si [51,88,127,189–194], (b) ZnO [53,68,92,94,195], and (c) SiC. (Reprinted with permission from Cheng et al. [196]. Copyright 2014 by American Chemical Society.) (d) Ag [102,168–170,197,198] and (e) Cu. (Reprinted with permission from Richter et al. [52]. Copyright 2009 by American Chemical Society.)

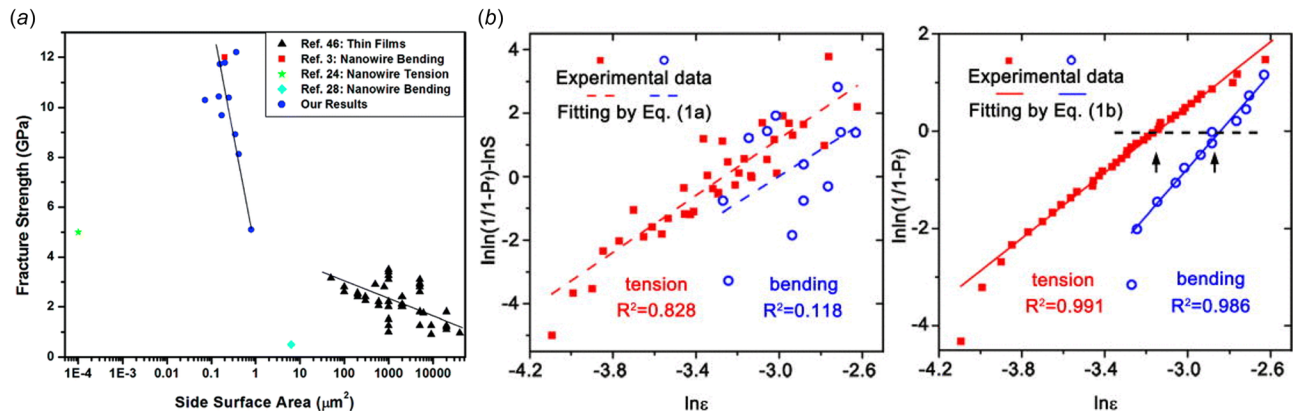


Fig. 12 (a) Fracture strength of Si NWs and thin films as a function of side surface area. (Reprinted with permission from Zhu et al. [51]. Copyright 2009 by American Chemical Society.) (b) Weibull statistics applied to fracture strength data of ZnO NWs correlating to surface area (left) and point defects (right). (Reprinted with permission from He et al. [210]. Copyright 2011 by American Institute of Physics).

leading Shockley partial dislocations activated at one nucleation site on the side surface, which agreed well with MD prediction [197] (Fig. 13(b)).

For single-crystalline Au NWs, Seo et al. reported a superplastic deformation induced by coherent twin propagation, which converted the initial  $\langle 110 \rangle$ -oriented NW with a rhombic cross section and  $\{111\}$  side facets to a  $\langle 100 \rangle$ -oriented NW with a rectangular cross section and  $\{100\}$  side facets [179] (Fig. 13(c)). The observed twinning mechanism for  $\langle 110 \rangle$ -oriented Au NWs under tension agreed well with the prediction based on the Schmid factors and generalized stacking fault energies [36]. The superplastic deformation was preceded by an abrupt stress drop. Sedlmayr et al. also reported deformation twinning as the dominant deformation mechanism for single-crystalline Au nanowhiskers (NWs), but in two different modes: (1) formation of a large number of small twins distributed along the length of the whisker or (2) the

formation of one long twin [220]. These two deformation modes corresponded to two different types of stress–strain behaviors, with continuous flow and pronounced stress drops, respectively.

Nanotwinned metals in bulk polycrystalline or thin-film forms have been investigated extensively [221,222]. NWs with twin boundaries (TBs) have recently received attention; the TBs can be perpendicular, inclined, or parallel to the NW length direction [160,178,223–225]. Effective hardening due to perpendicular TBs requires uniformly small twin spacing across the entire length of NWs [225], while inclined TBs are prone to detwinning driven by the finite resolved shear stress on the inclined TBs, leading to reduced strength [178].

Pentatwinned NWs are a special type of twinned NWs, containing a fivefold twinned nanostructure with five TBs along  $\{111\}$  planes in parallel to the NW axis and five surface facets of  $\{100\}$  planes. For pentatwinned Ag NWs, a dislocation-mediated, time-

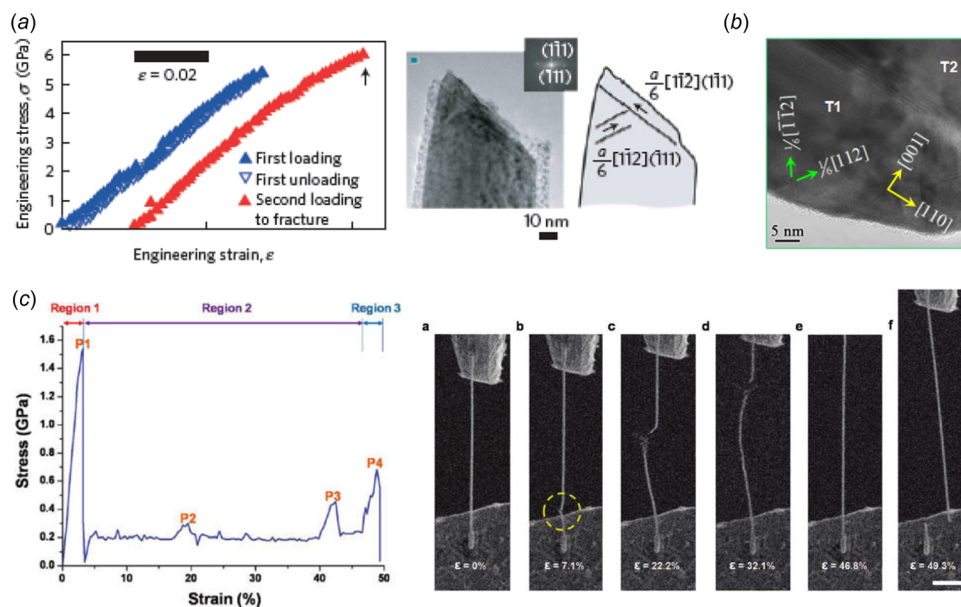


Fig. 13 (a) Stress–strain curve (left) and TEM image of the fracture surface (right) of a Pd NW. (Reprinted with permission from Chen et al. [218]. Copyright 2015 by Nature Publishing Group.) (b) TEM image showing two partial dislocations. (Reprinted with permission from Narayanan et al. [197]. Copyright 2015 by American Chemical Society.) (c) Stress–strain curve (left) and a sequence of SEM images showing the twin propagation and superplasticity (right) of a Au NW. (Reprinted with permission from Seo et al. [179]. Copyright 2011 by American Chemical Society).

dependent, and fully reversible plastic behavior was recently reported [55]. Figure 14(a) shows the stress–strain response in a typical tensile test of a pentatwinned Ag NW in four steps: loading, relaxation, unloading, and recovery. During the relaxation step, the stress decreased with time while the strain increased. During the recovery step, the plastic strain in the NW completely recovered with time. The stress relaxation was attributed to the surface dislocation nucleation and propagation, while the recovery of plastic strain was due to the retraction of partial dislocations. The TBs and the intrinsic stress field associated with the pentatwinned structure promoted retraction of partial dislocations, resulting in full plastic strain recovery. The dislocation/TB interaction mechanism was also conducive to the Bauschinger effect that was observed for the pentatwinned Ag NWs under cyclic loading [53] (Fig. 14(b)). Similar recoverable plasticity was also predicted to occur in bitwinned metallic NWs, where only one coherent TB runs in parallel to the NW axial direction [55]. Bauschinger effect was reported in thin films and NWs due to several mechanisms including heterogeneous distribution of grain size [226,227], dislocation–grain boundary interaction [228], surface passivation [229,230], or twinning–detwinning transition [231]. Note that for the observed recoverable plasticity, the applied strain to the NWs was relatively small (<2%), and hence, the partial dislocations did not transmit across the TBs, which is essential for the recoverable plasticity [55].

Another effect of the pre-existing TBs in the pentatwinned NWs is pronounced strain hardening [168,169]. MD simulations showed that such strain hardening was critically controlled by TBs and pre-existing defects. Strain hardening was size

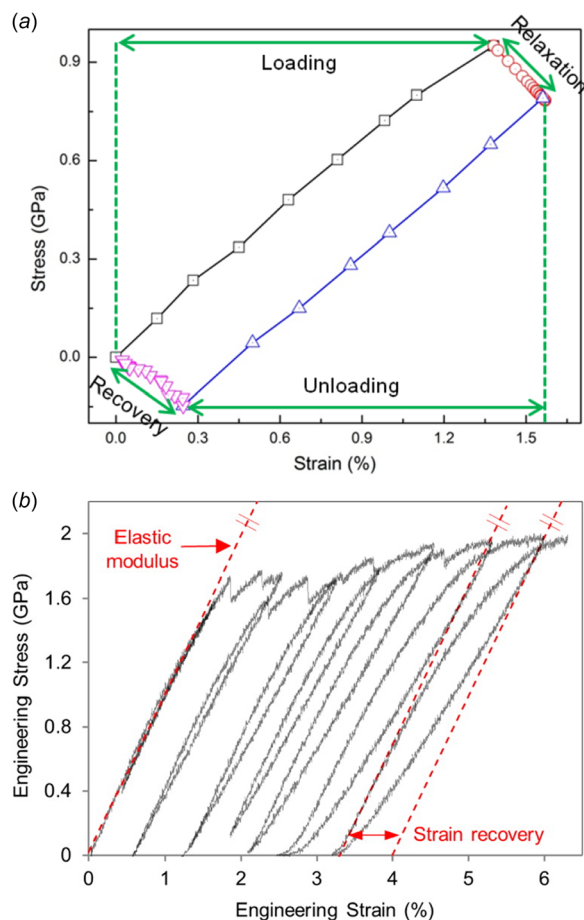


Fig. 14 (a) Recoverable plasticity (from Ref. [55]) and (b) Bauschinger effect (Reprinted with permission from Bernal et al. [187]. Copyright 2015 by American Chemical Society.) for pentatwinned Ag NWs.

dependent—thinner NWs achieved more hardening and higher ductility. The size-dependent strain hardening was originated from the obstruction of surface-nucleated dislocations by the TBs. This work showed that the statistical variation of source strengths of surface-nucleated dislocations plays an important role in mechanical properties of small-sized structures [197].

While surface dislocation nucleation is widely accepted for metal NWs, the origin of the dislocation nucleation remains elusive. Recently, an increasing body of evidence suggested that nucleation of a first dislocation in a defect-free crystal is assisted by diffusion of point defects [55,218,232–234]. Of note is that the relaxation behavior in the pentatwinned AgNWs as described above was not observed in single-crystalline Ag NWs [55]. Such a difference was attributed to vacancy defects, which were possible to exist in pentatwinned Ag NWs as suggested by cross-sectional TEM images. MD simulations revealed that vacancy defects can reduce dislocation nucleation barrier at the free surface, facilitating stress relaxation [55]. Chen et al. recently reported a strong temperature dependence of strength and its associated scatter in single-crystalline Pd NWs. The authors suggested a surface diffusion mechanism as the rate-limiting step for promoting dislocative activity [218]. In both studies, diffusion of point defects played a key role in aiding dislocation nucleation from free surfaces. However, the exact nature of the diffusion process and its effect on dislocation nucleation are still unclear and warrant further investigation.

**3.4 Anelasticity.** A number of anelastic mechanisms could be present in single-crystalline materials, including thermoelastic relaxation, piezoelectric coupling, and relaxations involving point defect motion [235–237]. At macroscopic scale, however, anelasticity is usually very small and negligible, especially in single-crystalline materials. As an example, anelasticity has been observed in bulk samples with hydrogen (or its isotope) as the most mobile interstitial species [238], with anelastic strain less than  $10^{-6}$ .

Recently, point defect induced giant anelasticity in single-crystalline ZnO and p-doped Si NWs was discovered under bending [101]. Such NWs can exhibit anelastic behavior that is up to 4 orders of magnitude larger than the largest anelasticity observed in bulk materials, with a recovery time-scale in the order of minutes. For a single NW, in situ SEM testing found that upon removal of the bending load, a substantial portion of the total strain gradually recovers following instantaneous recovery of the elastic strain (Fig. 15). The observed anelasticity was attributed to stress-gradient-induced migration of point defects [101]. The loading–unloading behavior of the NWs under buckling exhibited significant hysteresis and energy dissipation (Fig. 6(a)). Similar anelasticity was observed in GaAs [239] and CuO NWs [240], which was attributed to the crystalline defects and cooperative motion of twin-associated atoms, respectively.

## 4 Mechanical Applications of Nanowires

One-dimensional nanostructures including NWs have found a wide spectrum of mechanics-related applications, with several representative applications summarized below. In addition, like microelectronics many other NW applications involve temperature cycling that introduces thermal stress, such as solar cells and thermoelectric generators. Mechanics also plays a critical role in the reliability of such applications.

**4.1 Flexible and Stretchable Electronics.** Semiconductor NWs have been widely used as flexible device components in many areas including electronics, sensors, and optoelectronics [241–244]. NW transistors are of particular interest because of their high carrier mobilities compared with bulk or thin-film transistors made from the same materials. Fully transparent NW transistors based on  $\text{In}_2\text{O}_3$  and ZnO NWs for transparent and flexible electronics have been reported [242]. Ge/Si NW arrays with superior carrier mobility were printed to fabricate field-effect

transistors; the channel width can range from a single NW ( $\sim 30$  nm) up to  $250\ \mu\text{m}$  with a channel length on the order of  $\mu\text{m}$  [241], as shown in Fig. 16(a). NWs are considered to be outstanding candidates for chemical and biological sensing due to (1) their large surface-to-volume ratio and (2) dominant role of surface electrostatics on the carrier conduction due to their small radius that are comparable to the Debye screening length [247]. The NW sensors exhibited parts-per-billion sensitivity to  $\text{NO}_2$ . Individual ZnO NWs have been used as flexible strain sensors based on the piezotronic effect [248]. Photodetection with significantly higher sensitivities than their bulk counterparts was reported, which was attributed to their higher density of surface states (as a result of the high surface-area-to-volume ratio). The surface states were found to trap the photogenerated holes, therefore effectively increasing the electron-carrier lifetime and enhancing the observed photocurrent [241]. While a scalable and parallel process was developed for transferring hundreds of pre-aligned, top-down fabricated Si NWs onto plastic to yield highly ordered films for low-power sensor chips [243], in general large-scale alignment of NWs and transfer printing to different types of substrates remains a significant challenge.

Metal NWs have been used as transparent and sometimes flexible electrodes (or conductors) as an alternative to ITO [249,250], with excellent performances in terms of the combination of low sheet resistance, high transparency, and high flexibility. Scardaci et al. spray deposited Ag NWs over large areas to form networks with transmittance of 90% and sheet resistance of  $50\ \Omega/\square$  [251]. Yu et al. reported large flexibility of Ag NW film on a polymer substrate; the resistance remained nearly constant under compressive strain while increased by 2.9 times at a tensile strain of 16% [252].

Despite the tremendous progress of NW-based flexible electronics, wearable electronics that can deform in response to human motion and be conformal to curvilinear human skin requires a certain level of stretchability [254]. Microfabricated structures have been widely used in stretchable electronics, where buckling of such structures can lead to remarkable stretchability [254–256]. Alternatively, bottom-up synthesized nanomaterials have received much recent attention for stretchable electronics [13,257], including CNTs, graphene, NWs, and nanoparticles. For example, Si NWs have been explored for stretchable electronics [245,258,259]. Si NWs were transferred to a prestrained polydimethylsiloxane (PDMS) substrate and buckled upon release of the prestrain in the substrate. Interestingly, the NWs buckled into not only the wavy shape as commonly seen in the thin films or micro-ribbons but also the 3D coiled shape (Fig. 16(b)); the buckling shape was dictated by interfacial strength between PDMS and Si NWs and elastic modulus of the PDMS substrate, which can be tailored by surface treatment of the PDMS substrate [81,245]. The 3D coiled shape can be more stretchable than the wavy shape.

Recently, NW-based stretchable conductors and related sensors have attracted increasing attention for wearable applications [12–14,260,261]. As an example, AgNW conductors have been fabricated by embedding the AgNW network below the surface of an elastomeric substrate (e.g., PDMS). The AgNWs can be printed into different shapes and patterns. The AgNW/PDMS composite is highly conductive (conductivity  $>5000\ \text{S/cm}$ ) and higher stretchable ( $>50\%$  strain with constant conductivity). In addition, the AgNW network is below the PDMS surface, thus making the conductor mechanically robust without delamination and cracking [12]. Figure 15(c) shows the electric resistance of the AgNW conductors versus the tensile strain and the proposed mechanism for the constant resistance under large strain. These highly stretchable conductors can be used as conformal, wearable electrodes for bio-electronic sensing [261,262]. In the case of electrocardiogram electrodes, the AgNW dry electrodes outperformed the conventional wet Ag/AgCl electrodes with less motion artifacts. Note that the AgNW electrodes did not use the electrolytic gel, which made them suitable for long-term wearing. Such stretchable conductors have been used to make capacitive sensors [246,263] and antennas [264]. The capacitive sensors can detect strain (up to 50%), pressure, and finger touch. Figure 16(d) shows a wearable pressure sensor array. The strain sensors were used in several wearable applications including monitoring thumb movement, sensing the strain of the knee joint in patellar reflex (knee-jerk), and other human motions such as walking, running, and jumping from squatting, demonstrating the promising potential of using such sensors in robotic systems, prosthetics, health monitoring, and flexible touch panels [246].

For NW-based flexible and stretchable electronics, a key issue is interface mechanics between NWs and substrate, especially under large deformation, considering the magnitude difference of about 5 orders in their Young's moduli. For instance, interface sliding was observed between Si NWs and PDMS substrate [245]; with surface treatment of the PDMS substrate, the static friction (interfacial strength) increased [81] and the interface sliding was largely suppressed. The interface sliding played an important role in the NW buckling shape [265,266]. Shear-lag models have been used to analyze the shear stress transfer between graphene and substrate [267,268], which can be extended to NWs and substrate too. Another key issue is fatigue of the NWs as the flexible and stretchable electronic devices are expected to undergo a large number of tension and compression cycles [269].

**4.2 Nanocomposites.** CNTs have been widely used in nanocomposites, improving their mechanical and other multifunctional properties [3,270]. Crystalline NWs could also contribute to enhance mechanical properties of nanocomposites due to their

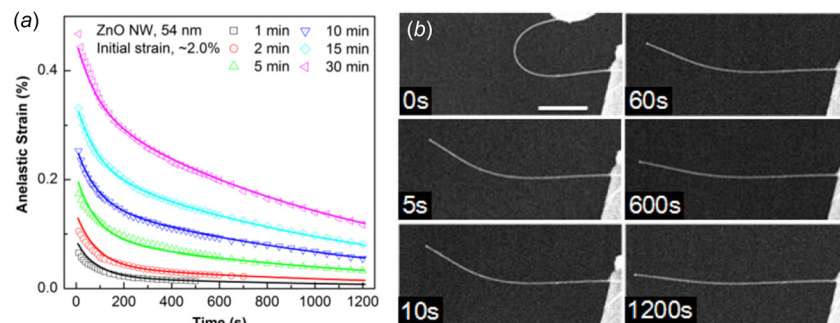


**Fig. 15** (a) Anelastic strain as a function of recovery time for six different durations of holding time. The NW diameter was 54 nm and the initial bending strain was 1.94%. (b) A sequence of SEM images showing the recovery process of a ZnO NW after the bending load was removed. Scale bar:  $2\ \mu\text{m}$ . (Reprinted with permission from Cheng et al. [101]. Copyright 2015 by Nature Publishing Group).

exceptional mechanical properties [196]. Indeed nanocomposites incorporating crystalline NWs are commonly used to attain highly conductive and highly stretchable conductors, as reviewed in Sec. 4.1. In this section, emphasis is placed on mechanical nanocomposites [271].

Yang et al. fabricated SiC NW-reinforced SiC matrix composites. With the incorporation of ~6 vol. % randomly oriented single-crystal SiC NWs in the matrices, the fracture toughness and flexural strength of the composites were found to double. The reinforcement efficiency of the NWs was attributed to the carbon coating around the NWs that could serve as the NW/matrix interfacial layer [272]. The authors further investigated the effect of the volume fraction of the SiC NWs, up to 6.1%. They found that the flexural (bending) modulus, proportional limit, and ultimate strength increase linearly with the increasing NW volume fraction. Specifically, the flexural properties depended on the thickness of carbon coating on the NWs [273].

Rao and coworkers found a significant increase of the stiffness and strength of semicrystalline polyvinyl alcohol due to incorporation of SiC and Al<sub>2</sub>O<sub>3</sub> NWs, even with a small vol. % addition of the NWs [274]. The increase in the stiffness was attributed to crystallization of the polymer induced by the NWs, the surface-to-volume ratio of the NWs, and the possible in-plane alignment of the NWs. The strengthening was attributed to pull-out of the NWs.

NWs have also been used in coating materials. A SiC NW-toughened SiC coating with homogeneously dispersed NWs within the coating was prepared on C/C composites [275]. The fracture toughness of the SiC NWs-toughened SiC coating was found to be about 48% higher than that of the pure SiC coating. Such an increase was attributed to several toughening mechanisms such as NW pullout, NW bridging, and crack deflection. In addition, the SiC NWs-toughened SiC coating was found to drastically enhance the oxidation resistance for the C/C composites. Fu et al. used SiC NWs as reinforcements in a joint material, leading to marked increase in the shear strength [276].

For nanocomposites, a central mechanics issue is the interface mechanics between nanomaterials and matrix [277]. CNT-based nanocomposites have been intensively investigated [278,279]. Single CNT pull-out experiment has been used to measure the

interfacial strength [280–282]. The experimental setup used for conducting tensile testing inside SEM (see Sec. 2.2.2) can be easily adapted to perform pull-out tests on single NWs from the matrix.

**4.3 Nanoelectromechanical Systems.** One-dimensional nanostructures have been explored for NEMS switches [283,284]. Han et al. reported an NW mechanical switch with a built-in diode [285]. The Si NW switch was fabricated by the top-down approach. Li et al. reported NEMS switches consisting of VLS-grown Si NWs suspended over metal electrodes [286]. The device operated as a transistor with the suspended part of the NW bent to touch the metal electrode via electrostatic force. Feng et al. reported electrostatically actuated, contact-mode NEMS switches based on very thin SiC NWs, with NW widths as small as ~20 nm and lateral switching gaps as narrow as ~10 nm [287]. These NWs were lithographically patterned from a 50 nm thick SiC layer heteroepitaxially grown on single-crystal Si. The switches possessed very low switch-on voltages (from a few volts down to ~1 V) and high on/off ratios ( $>10^2$  or  $10^3$ ).

Husain et al. reported the fabrication and measurement of a platinum NW resonator [288]. This device was among the smallest NEMS reported. It had a fundamental vibration frequency of 105.3 MHz with a *Q*-factor of 8500 at 4 K. SiC nanoresonators are capable of yielding substantially higher frequencies than GaAs and Si counterparts for given dimensions [9].

In the above nanoresonators, the NWs were top-down fabricated lithographically. Bottom-up synthesized NWs have also been used in nanoresonators in two ways. Yang and coworkers developed a technique to directly synthesize doubly clamped, single-crystalline (111) Si NWs in lithographically defined micro-trenches on silicon-on-insulator substrates [289]. Such as-synthesized, suspended NWs can function as high-frequency nanoresonators without the need of further device processing. Li et al. introduced a new bottom-up assembly method to fabricate large-area NEMS arrays; each array had over 2000 single NW resonators [290]. The NWs were chemically functionalized before integrated onto a silicon chip at desired locations. The two types of cantilevered resonators using Si and Rh NWs had *Q*-factors of 4500 and 1150, respectively, in vacuum.

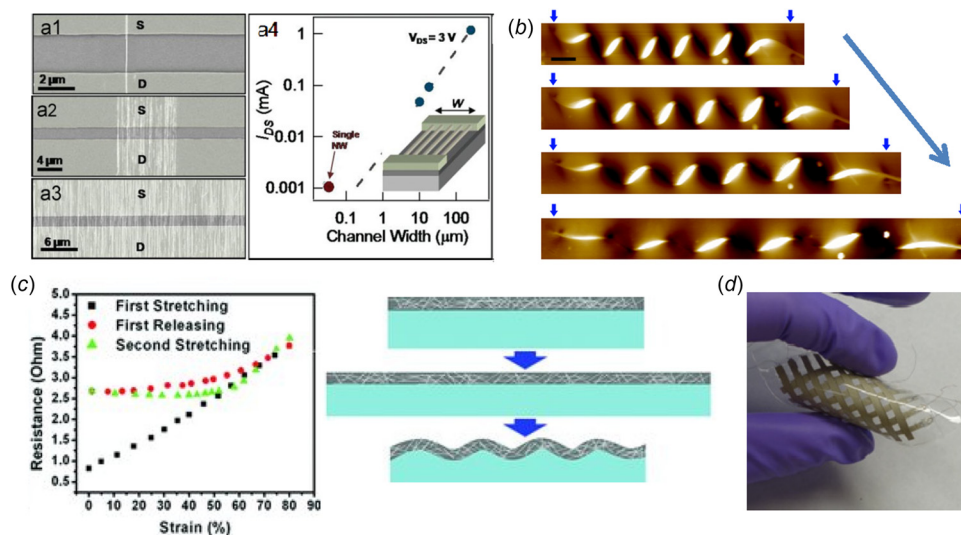


**Fig. 16** (a) Field-effect transistors based on Ge/Si NW arrays with different channel widths that can be printed on flexible substrates. (Reprinted with permission from Fan et al. [261]. Copyright 2009 by Wiley.) (b) A 3D coiled Si NW (due to buckling) under stretching. (Reprinted with permission from Xu et al. [245]. Copyright 2011 by American Chemical Society.) (c) Resistance as a function of applied strain during loading, unloading, and reloading (left) and the schematic of the corresponding mechanism. (Reprinted with permission from Xu and Zhu [12]. Copyright 2012 by Wiley.) (d) A pressure sensor array. (Reprinted with permission from Yao and Zhu [246]. Copyright 2014 by Royal Society of Chemistry).

Poncharal et al. demonstrated using the shift of the resonant frequency of a vibrating cantilevered CNT to estimate the mass of a particle attached to the end of the CNT [46]. Using the same concept, Huang et al. estimated the mass of 3.3 fg particle attached to the end of a ZnO NW based on the shift of its resonance frequency [291]. Roukes and coworkers demonstrated zeptogram-scale mass sensing using their NEMS resonators [292]. In the mass sensing applications, the resonance frequencies of the NWs were typically detected by imaging or other external electromagnetic methods.

He et al. demonstrated for the first time self-transducing very high-frequency Si NW resonators based on piezoresistivity of the Si NWs [293]. Lou et al. reported a pressure sensor with a 200  $\mu\text{m}$  diaphragm using Si NWs as a piezoresistive sensing element, with relatively high sensitivity (0.6%/psi) and good linearity [294]. It is worth mentioning about the size effect on piezoresistivity of Si. He and Yang reported giant piezoresistivity Si NWs [295], while others reported that Si NWs possess the same piezoresistivity as bulk Si [136,296]. The piezoresistivity of Si NWs remains a matter of debate, with limited reproducible evidence for giant piezoresistivity in ungated NWs. But in gated NWs, giant piezoresistivity has been reproduced [297].

**4.4 Energy Applications.** A broad range of nanomaterials including crystalline NWs has been explored to achieve enhanced efficiency and lifetime in conversion and storage of the renewable energy resources. For example, piezoelectric NWs (e.g., ZnO) have been demonstrated to harvest mechanical energy using piezoelectric effect [5] and are being used in highly efficient dye-sensitized solar cells [6]; Si NWs have been used to harvest waste heat using thermoelectric effect [7,298] and can potentially serve as an excellent material as anodes in lithium-ion batteries [8].

Wang and Song demonstrated harvesting mechanical energy by deflecting individual ZnO NWs with a conductive AFM tip in contact mode [5] (Fig. 17(a)). The coupling of piezoelectric and semiconducting properties in ZnO enabled charge separation across the NW when the NW was bent. The rectifying characteristic of the Schottky barrier formed between the metal tip and the NW was a key factor for electrical current generation. The efficiency of the NW-based piezoelectric power generator was estimated to be 17–30%. Later the Wang group extended this concept to a variety of piezoelectric NWs in different device configurations for a broad range of self-powered applications [299–301].

Electromechanical coupling of piezoelectric NWs plays an important role in energy harvesting based on such NWs. Agrawal and Espinosa found giant size effect in piezoelectric constants in ZnO and GaN NWs by a first principles investigation [302]. Such a size effect was attributed to the changes in local polarization as a result of charge redistribution near free surfaces. Dai et al. reported that even nonpiezoelectric materials may act as piezoelectric at the nanoscale because of surface effects [303]. Inversely surface piezoelectricity in addition to surface stress and

surface elasticity was found to affect the resonance frequency and buckling of piezoelectric NWs [304,305].

Chan et al. reported near theoretical specific capacity (4200 mAh  $\text{g}^{-1}$ ) for VLS-grown Si NW anodes on a stainless steel current collector [8] (Fig. 17(b)). Si is regarded as an attractive anode material for lithium batteries because it has a low discharge potential and the highest known theoretical charge capacity, but Si anodes typically suffer from volume changes by 400% upon insertion and extraction of lithium which can result in pulverization and capacity fading [306]. Chan et al. found the Si NWs can accommodate large strain without pulverization [8].

Huang et al. reported the in situ TEM observation of the lithiation of a single  $\text{SnO}_2$  NW during electrochemical charging [307]. Upon charging, the authors found that a reaction front propagated progressively along the NW, causing the NW to swell, elongate, and spiral. The reaction front contained a high density of mobile dislocations with continuous nucleation and absorption. This dislocation cloud was deemed as a structural precursor to electrochemically driven amorphization. As suggested by the authors, lithiation-induced volume expansion, plasticity, and pulverization of electrode materials are the major mechanics issues that degrade the performance and lifetime of high-capacity anodes in lithium-ion batteries. Extensive studies have been reported to understand the mechanistic insight for the design of NW-based advanced batteries [308–311].

**4.5 Strain Engineering.** Elastic strain engineering can be utilized to tune the fundamental properties of semiconductor materials [1]. As an example, the so-called strained silicon technology is ubiquitously used in the semiconductor industry as a way to enhance the charge carrier mobility. Nanostructures including NWs can withstand a much larger range of elastic strain than their bulk counterparts, which make them attractive for elastic strain engineering. Indeed, elastic strain engineering of semiconductor NWs has received much interest recently. So far, three methods have been used to introduce strain in the NWs: buckling an NW on a stretchable substrate [245], bending an NW on a substrate [15,312,313], and stretching a freestanding NW [314].

Agrawal and coworkers buckled CdS NWs by transferring them onto a prestrained PDMS substrate followed with releasing the prestrain [315], similar to the procedure used to create 3D coiled Si NWs [245]. PL measurements showed periodic bandgap modulation along the wavy NW with bandgap shifts as large as 250 meV. Polarized PL and reflectance measurements on single NWs were used to characterize the shift behavior of A- and B-excitons as a function of strain (Fig. 18(a)).

Han et al. reported a red shift of the exciton of ZnO NWs caused by bending strain, measured by a CL spectroscopy at low-temperature (81 K) [313]. Chen et al. observed variations in the optical phonon frequency along the bent InP NWs using Raman spectroscopy. Theory showed that compressive and tensile strain

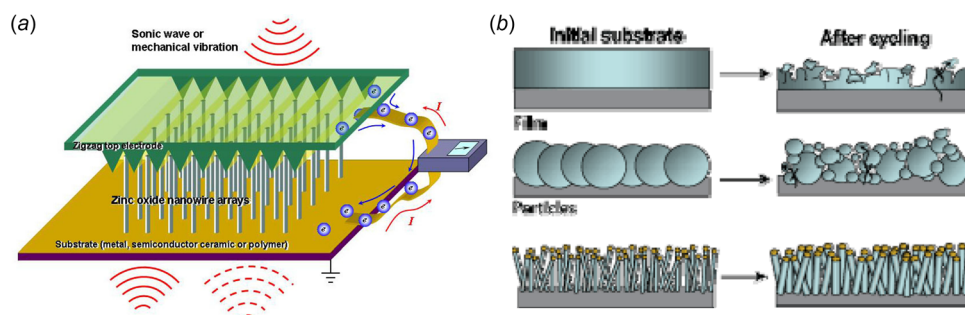


**Fig. 17 (a)** Piezoelectric energy harvesting based on an array of ZnO NWs. (Reprinted with permission from Wang and Song [5]. Copyright 2006 by American Association for the Advancement of Science). **(b)** Si NW anodes exhibited near theoretical specific capacity. (Reprinted with permission from Chan et al. [8]. Copyright 2008 by Nature Publishing Group).

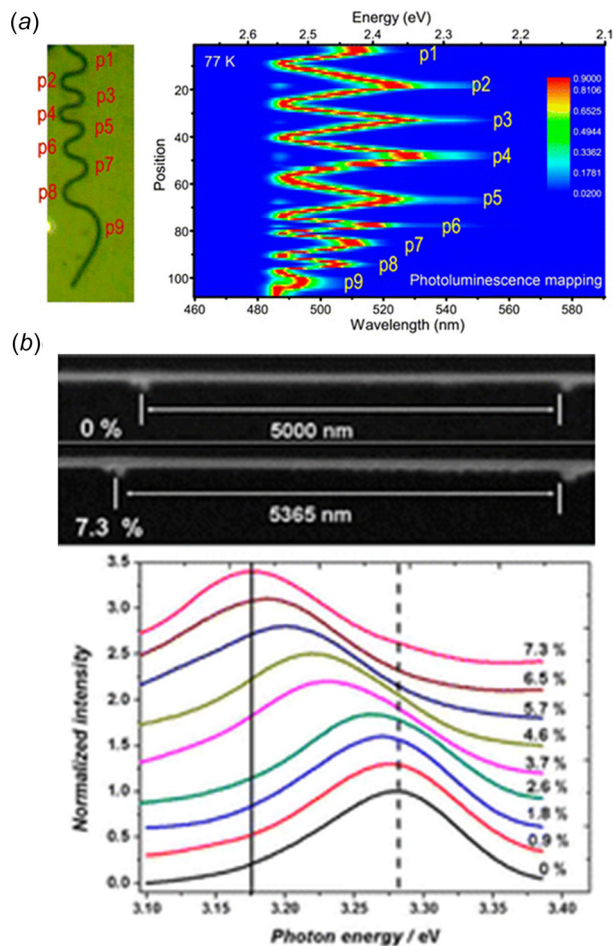


**Fig. 18** (a) Optical image of a buckled CdS NW (left) and the corresponding PL mapping (right). (Reprinted with permission from Sun et al. [315]. Copyright 2013 by American Chemical Society.) (b) A single ZnO NW under tension in SEM (top) and the CL signal as a function of the applied strain. (Reprinted with permission from Wei et al. [314]. Copyright 2012 by American Chemical Society).

inside the NWs is the physical origin of the observed phonon energy variations [312]. Grumstrup et al. characterized charge-carrier recombination and transport dynamics in locally bent Si NWs by pump-probe microscopy with femtosecond temporal

resolution and submicron spatial resolution [15]. The electron-hole recombination rate was found to increase sixfold under 5% strain. The changes in recombination rate were reversible upon reduction of the applied strain, indicating the change of electronic structure associated with elastic strain rather than introduction of defects.

Wei et al. reported the size-dependent bandgap modulation of ZnO NWs under tensile strain [314]; the strain was applied by an in situ SEM tensile testing while the bandgap was measured setup by a CL spectroscopy in the SEM (Fig. 18(b)). As the fracture strain increased with decreasing NW size, the bandgap variation increased too. The authors attributed the pronounced size effect of strained NWs on the bandgap variation to a competition between core-dominated and surface-dominated bandgap modulations [314].

## 5 Summary and Outlook

This review provides a summary of recent advances in mechanics of crystalline NWs focusing on the experimental aspects. Many different types of experimental methods, mostly based on AFM or electron microscopes, have been developed and employed to measure mechanical behaviors of 1D nanostructures including metal, semiconductor, and ceramic NWs. A wealth of mechanics topics of crystalline NWs has been investigated experimentally including elasticity, fracture, plasticity, and anelasticity, often in conjunction with atomistic simulations. The effects of free surfaces and more recently internal defects were found to play a dominant role in the mechanical behaviors. Crystalline NWs have been widely used in many applications, some of which are directly related to their mechanical properties such as flexible/stretchable electronics, nanocomposites, NEMS, energy harvesting/storage, and strain engineering.

Mechanical testing of crystalline NWs remains a challenging task. Much of the early results on property measurements showed significant scatter and discrepancy, which is not totally surprising considering the infancy of the field, limitation in the accuracy of the testing methods, and probable differences in many factors such as the sample cross sections and microstructures (related to the synthesis methods and conditions), loading modes, and boundary conditions. As an example, the NW cross section might vary with the diameter, which can have important impact on the measured mechanical properties [102]. For these reasons, this review does not aim to provide a comprehensive list of the available data; rather it focuses on major experimental methods including operating principles and pros and cons and key findings on the mechanics of crystalline NWs from such experimental studies. With continued advance in testing methods and careful consideration of

**Table 1 Comparison of AFM-based testing methods**

AFM-based testing methods	Mechanics theory	Resolution	Pros	Cons
Contact mode	Beam theory (Eq. (1))	0.02 nm displacement; 0.2 nN force (typical stiffness $\sim 10$ N/m) [326]	High displacement and force resolution	Possible "slippage" of AFM tip off NW
Lateral force mode	Beam theory (Eq. (1))	0.2 nm displacement; 20 nN force (typical stiffness $\sim 100$ N/m) [42,326]	Mitigation of possible slippage	Lower resolution; force calibration is more challenging
Indentation mode	Hertz contact theory (Eq. (2))	Same as contact mode	Experiment is relatively simple	Data extraction is complicated (Hertz contact theory might not apply, substrate effect); possible slippage
Contact resonance mode	Dynamic beam equation (4) + Hertz contact theory (Eq. (3))	0.01 kHz resonance frequency [327]	Experiment is relatively simple	Data extraction is complicated (depending on accurate AFM cantilever dynamic analysis; Hertz contact theory might not apply)

the factors mentioned above, more consistent testing results have been and will continue to be obtained. For example, efforts have been taken to systematically examine the influences of sample cross sections [102] and microstructures [55,187,225], loading modes [53,102], and boundary conditions [61,62].

In addition to accurate measurement of the mechanical properties (e.g., Young's modulus, yield strength, and fracture strength), measuring more advanced behaviors and probing deformation mechanisms have received more and more attention recently. The advanced behaviors are related to the dependence of testing temperature, rate, time, environment, etc. For instance, creep, stress relaxation, and fatigue properties are of relevance to the long-term reliability of the nanodevices with crystalline NWs as the constituents. Effects of strain rate and temperature on the mechanical properties are important during the device operation. Measuring these properties demands the development of novel experimental methods. MEMS-based methods have shown particular promise in meeting this need. For example, MEMS testing stages have been developed to measure mechanical properties of NWs at high temperature [54] and high strain rate [56], in conjunction with SEM and TEM. The advances in experimental methods, on the other hand, will facilitate investigation to understand the deformation mechanisms. For example, strain rate, temperature, and relaxation transient tests can be used to probe thermally activated mechanisms; temperature tests can help understand the mechanism(s) behind brittle to ductile transition as a function of the sample size. TEM is the most powerful tool in elucidating the deformation mechanisms. With the recent advances in time-resolved electron microscopy [316] (e.g., dynamic transmission electron microscopy (DTEM) [317]), it might become possible to capture the defect dynamics of crystalline NWs with atomic resolution, perhaps in conjunction with an MEMS-based testing stage.

Beyond the SEM, TEM, AFM, and optical microscopes, it is promising to combine nanomechanical testing with spectroscopy for multiphysical testing. For instance, micro-Raman has been used to measure temperature and stress with spatial resolution around 1  $\mu\text{m}$ ; PL can be used to measure bandgap of semiconductors.

Nanostructures have received extensive interests in the last two to three decades, primarily due to their outstanding properties and the fact that they can provide an ideal platform for probing fundamental science at the nanoscale. To sustain a high level of interest in nanostructures, large-scale applications and how to create materials, devices, and systems for such applications (i.e., scalable manufacturing) must be rigorously sought, where mechanics can also play a valuable role. For example, in the cases of flexible/stretchable electronics and nanocomposites, interfacial mechanics between nanostructures and substrates (or matrices) is of particular relevance in view of the large surface-to-volume ratio of the nanostructures [81,245,258,318–320]. To manufacture flexible and stretchable devices, adhesion plays a key role in the contact transfer printing [241,321], and interfacial shear stress transfer can facilitate alignment of 1D nanostructures [318,322]. In addition to composites, architected materials enabled by additive manufacturing have shown promises to link the outstanding nanoscale material properties to large-scale structural behaviors [323–325], as in many biomaterials self-assembled, hierarchical arrangement of different structural elements at their relevant length scales can lead to superior properties [328].

## Acknowledgment

The financial support by the National Science Foundation (NSF) through Award Nos. CMMI-1301193 and DMR-1410475 is gratefully acknowledged. The author would like to thank H. Gao and T. Zhu for valuable discussions, W. Lu, Y. Gu, G. Richter, H. Huang, B. Wiley, and Z. L. Wang for providing the NW samples that enabled the nanomechanics study in the author's group, and T.-H. Chang for helping prepare several figures.

## References

- [1] Zhu, T., and Li, J., 2010, "Ultra-Strength Materials," *Prog. Mater. Sci.*, **55**, pp. 710–757.
- [2] Suresh, S., and Li, J., 2008, "Materials Science Deformation of the Ultra-Strong," *Nature*, **456**, pp. 716–717.
- [3] Baughman, R. H., Zakhidov, A. A., and de Heer, W. A., 2002, "Carbon Nanotubes—The Route Toward Applications," *Science*, **297**, pp. 787–792.
- [4] Xu, F., Wang, X., Zhu, Y. T., and Zhu, Y., 2012, "Wavy Ribbons of Carbon Nanotubes for Stretchable Conductors," *Adv. Funct. Mater.* **22**(6), pp. 1279–1283.
- [5] Wang, Z. L., and Song, J. H., 2006, "Piezoelectric Nanogenerators Based on Zinc Oxide Nanowire Arrays," *Science*, **312**(5771), pp. 242–246.
- [6] Law, M., Greene, L. E., Johnson, J. C., Saykally, R., and Yang, P. D., 2005, "Nanowire Dye-Sensitized Solar Cells," *Nat. Mater.*, **4**, pp. 455–459.
- [7] Hochbaum, A. I., Chen, R. K., Delgado, R. D., Liang, W. J., Garnett, E. C., Najarian, M., Majumdar, A., and Yang, P. D., 2008, "Enhanced Thermoelectric Performance of Rough Silicon Nanowires," *Nature*, **451**, pp. 163–167.
- [8] Chan, C. K., Peng, H. L., Liu, G., McIlwrath, K., Zhang, X. F., Huggins, R. A., and Cui, Y., 2008, "High-Performance Lithium Battery Anodes Using Silicon Nanowires," *Nat. Nanotechnol.*, **3**, pp. 31–35.
- [9] Yang, Y. T., Ekinci, K. L., Huang, X. M. H., Schiavone, L. M., Roukes, M. L., Zorman, C. A., and Mehregany, M., 2001, "Monocrystalline Silicon Carbide Nanoelectromechanical Systems," *Appl. Phys. Lett.*, **78**(2), pp. 162–164.
- [10] Lee, J.-Y., Connor, S. T., Cui, Y., and Peumans, P., 2008, "Solution-Processed Metal Nanowire Mesh Transparent Electrodes," *Nano Lett.*, **8**(2), pp. 689–692.
- [11] De, S., Higgins, T. M., Lyons, P. E., Doherty, E. M., Nirmalraj, P. N., Blau, W. J., Boland, J. J., and Coleman, J. N., 2009, "Silver Nanowire Networks as Flexible, Transparent, Conducting Films: Extremely High DC to Optical Conductivity Ratios," *ACS Nano*, **3**(7), pp. 1767–1774.
- [12] Xu, F., and Zhu, Y., 2012, "Highly Conductive and Stretchable Silver Nanowire Conductors," *Adv. Mater.*, **24**(37), pp. 5117–5122.
- [13] Yao, S., and Zhu, Y., 2015, "Nanomaterial-Enabled Stretchable Conductors: Strategies, Materials and Devices," *Adv. Mater.*, **27**(9), pp. 1480–4511.
- [14] Lee, P., Lee, J., Lee, H., Yeo, J., Hong, S., Nam, K. H., Lee, D., Lee, S. S., and Ko, S. H., 2012, "Highly Stretchable and Highly Conductive Metal Electrode by Very Long Metal Nanowire Percolation Network," *Adv. Mater.*, **24**(25), pp. 3326–3332.
- [15] Grumstrup, E. M., Gabriel, M. M., Pinion, C. W., Parker, J. K., Cahoon, J. F., and Papanikolas, J. M., 2014, "Reversible Strain-Induced Electron-Hole Recombination in Silicon Nanowires Observed With Femtosecond Pump-Probe Microscopy," *Nano Lett.* **14**(11), pp. 6287–6292.
- [16] Park, H. S., and Qian, X., 2010, "Surface-Stress-Driven Lattice Contraction Effects on the Extinction Spectra of Ultrasmall Silver Nanowires," *J. Phys. Chem. C*, **114**(19), pp. 8741–8748.
- [17] Wang, W., Yang, Q., Fan, F., Xu, H., and Wang, Z. L., 2011, "Light Propagation in Curved Silver Nanowire Plasmonic Waveguides," *Nano Lett.*, **11**(4), pp. 1603–1608.
- [18] Oliver, W. C., and Pharr, G. M., 1992, "An Improved Technique for Determining Hardness and Elastic-Modulus Using Load and Displacement Sensing Indentation Experiments," *J. Mater. Res.*, **7**(6), pp. 1564–1583.
- [19] Nix, W. D., 1989, "Mechanical-Properties of Thin-Films," *Metall. Trans. A: Phys. Metall. Mater. Sci.*, **20**, pp. 2217–2245.
- [20] Nix, W. D., and Gao, H., 1998, "Indentation Size Effects in Crystalline Materials: A Law for Strain Gradient Plasticity," *J. Mech. Phys. Solids*, **46**(3), pp. 411–425.
- [21] Greer, J. R., and De Hosson, J. T. M., 2011, "Plasticity in Small-Sized Metallic Systems: Intrinsic Versus Extrinsic Size Effect," *Prog. Mater. Sci.*, **56**(6), pp. 654–724.
- [22] Uchic, M. D., Shade, P. A., and Dimiduk, D. M., 2009, "Plasticity of Micrometer-Scale Single Crystals in Compression," *Annu. Rev. Mater. Res.*, **39**, pp. 361–386.
- [23] Volkert, C. A., and Lilleodden, E. T., 2006, "Size Effects in the Deformation of Sub-Micron Au Columns," *Philos. Mag.*, **86**(33–35), pp. 5567–5579.
- [24] Uchic, M. D., Dimiduk, D. M., Florando, J. N., and Nix, W. D., 2004, "Sample Dimensions Influence Strength and Crystal Plasticity," *Science*, **305**(5686), pp. 986–989.
- [25] Greer, J. R., Oliver, W. C., and Nix, W. D., 2005, "Size Dependence of Mechanical Properties of Gold at the Micron Scale in the Absence of Strain Gradients," *Acta Mater.*, **53**(6), pp. 1821–1830.
- [26] Weinberger, C. R., and Cai, W., 2008, "Surface-Controlled Dislocation Multiplication in Metal Micropillars," *Proc. Natl. Acad. Sci. U.S.A.*, **105**(38), pp. 14304–14307.
- [27] Tang, H., Schwarz, K., and Espinosa, H., 2007, "Dislocation Escape-Related Size Effects in Single-Crystal Micropillars Under Uniaxial Compression," *Acta Mater.*, **55**(5), pp. 1607–1616.
- [28] El-Awady, J., Woodward, C., Dimiduk, D., and Ghoniem, N., 2009, "Effects of Focused Ion Beam Induced Damage on the Plasticity of Micropillars," *Phys. Rev. B* **80**(1), p. 104104.
- [29] Guruprasad, P., and Benzerga, A., 2008, "Size Effects Under Homogeneous Deformation of Single Crystals: A Discrete Dislocation Analysis," *J. Mech. Phys. Solids*, **56**(1), pp. 132–156.
- [30] Oh, S. H., Legros, M., Kiener, D., and Dehm, G., 2009, "In Situ Observation of Dislocation Nucleation and Escape in a Submicrometre Aluminium Single Crystal," *Nat. Mater.*, **8**, pp. 95–100.
- [31] Diao, J., Gall, K., Dunn, M. L., and Zimmerman, J. A., 2006, "Atomistic Simulations of the Yielding of Gold Nanowires," *Acta Mater.*, **54**(3), pp. 643–653.

- [32] Park, H. S., Gall, K., and Zimmerman, J. A., 2006, "Deformation of FCC Nanowires by Twinning and Slip," *J. Mech. Phys. Solids*, **54**(9), pp. 1862–1881.
- [33] Zhu, T., Li, J., Samanta, A., Leach, A., and Gall, K., 2008, "Temperature and Strain-Rate Dependence of Surface Dislocation Nucleation," *Phys. Rev. Lett.*, **100**, p. 25502.
- [34] Zheng, H., Cao, A., Weinberger, C. R., Huang, J. Y., Du, K., Wang, J., Ma, Y., Xia, Y., and Mao, S. X., 2010, "Discrete Plasticity in Sub-10-nm-Sized Gold Crystals," *Nat. Commun.*, **1**, p. 144.
- [35] Qian, D., Wagner, G. J., Liu, W. K., Yu, M. F., and Ruoff, R. S., 2002, "Mechanics of Carbon Nanotubes," *ASME Appl. Mech. Rev.*, **55**(6), pp. 495–533.
- [36] Weinberger, C. R., and Cai, W., 2012, "Plasticity of Metal Nanowires," *J. Mater. Chem.*, **22**, pp. 3277–3292.
- [37] Park, H. S., Cai, W., Espinosa, H. D., and Huang, H., 2009, "Mechanics of Crystalline Nanowires," *MRS Bull.*, **34**(3), pp. 178–183.
- [38] Salvétat, J. P., Briggs, G. A. D., Bonard, J. M., Bacsa, R. R., Kulik, A. J., Stockli, T., Burnham, N. A., and Forro, L., 1999, "Elastic and Shear Moduli of Single-Walled Carbon Nanotube Ropes," *Phys. Rev. Lett.*, **82**, pp. 944–947.
- [39] Walters, D. A., Ericson, L. M., Casavant, M. J., Liu, J., Colbert, D. T., Smith, K. A., and Smalley, R. E., 1999, "Elastic Strain of Freely Suspended Single-Wall Carbon Nanotube Ropes," *Appl. Phys. Lett.*, **74**(25), pp. 3803–3805.
- [40] Li, X. D., Hao, H. S., Murphy, C. J., and Caswell, K. K., 2003, "Nanoindentation of Silver Nanowires," *Nano Lett.*, **3**(11), pp. 1495–1498.
- [41] Cuenot, S., Fretigny, C., Demoustier-Champagne, S., and Nysten, B., 2004, "Surface Tension Effect on the Mechanical Properties of Nanomaterials Measured by Atomic Force Microscopy," *Phys. Rev. B*, **69**, p. 165410.
- [42] Wu, B., Heidelberg, A., and Boland, J. J., 2005, "Mechanical Properties of Ultrahigh-Strength Gold Nanowires," *Nat. Mater.*, **4**, pp. 525–529.
- [43] Paulo, A. S., Bokor, J., Howe, R. T., He, R., Yang, P., Gao, D., Carraro, C., and Maboudian, R., 2005, "Mechanical Elasticity of Single and Double Clamped Silicon Nanobeams Fabricated by the Vapor-Liquid-Solid Method," *Appl. Phys. Lett.*, **87**(5), p. 53111.
- [44] Sohn, Y.-S., Park, J., Yoon, G., Song, J., Jee, S.-W., Lee, J.-H., Na, S., Kwon, T., and Eom, K., 2010, "Mechanical Properties of Silicon Nanowires Nanoscale," *Res. Lett.*, **5**(1), pp. 211–216.
- [45] Treacy, M. M. J., Ebbesen, T. W., and Gibson, J. M., 1996, "Exceptionally High Young's Modulus Observed for Individual Carbon Nanotubes," *Nature*, **381**, pp. 678–680.
- [46] Poncharal, P., Wang, Z. L., Ugarte, D., and de Heer, W. A., 1999, "Electrostatic Deflections and Electromechanical Resonances of Carbon Nanotubes," *Science*, **283**(5407), pp. 1513–1516.
- [47] Yu, M. F., Lourie, O., Dyer, M. J., Moloni, K., Kelly, T. F., and Ruoff, R. S., 2000, "Strength and Breaking Mechanism of Multiwalled Carbon Nanotubes Under Tensile Load," *Science*, **287**(5453), pp. 637–640.
- [48] Dikin, D. A., Chen, X., Ding, W., Wagner, G., and Ruoff, R. S., 2003, "Resonance Vibration of Amorphous SiO<sub>2</sub> Nanowires Driven by Mechanical or Electrical Field Excitation," *J. Appl. Phys.*, **93**(1), pp. 226–230.
- [49] Zhu, Y., and Espinosa, H. D., 2005, "An Electromechanical Material Testing System for In Situ Electron Microscopy and Applications," *Proc. Natl. Acad. Sci. U.S.A.*, **102**(41), pp. 14503–14508.
- [50] Chen, C. Q., Shi, Y., Zhang, Y. S., Zhu, J., and Yan, Y. J., 2006, "Size Dependence of the Young's Modulus of ZnO Nanowires," *Phys. Rev. Lett.*, **96**, p. 75505.
- [51] Zhu, Y., Xu, F., Qin, Q. Q., Fung, W. Y., and Lu, W., 2009, "Mechanical Properties of Vapor-Liquid-Solid Synthesized Silicon Nanowires," *Nano Lett.*, **9**(11), pp. 3934–3939.
- [52] Richter, G., Hillerich, K., Gianola, D. S., Mönig, R., Kraft, O., and Volkert, C. A., 2009, "Ultra High Strength Single Crystalline Nanowhiskers Grown by Physical Vapor Deposition," *Nano Lett.*, **9**(8), pp. 3048–3052.
- [53] Xu, F., Qin, Q., Mishra, A., Gu, Y., and Zhu, Y., 2010, "Mechanical Properties of ZnO Nanowires Under Different Loading Modes," *Nano Res.*, **3**(4), pp. 271–280.
- [54] Chang, T.-H., and Zhu, Y., 2013, "A Microelectromechanical System for Thermomechanical Testing of Nanostructures," *Appl. Phys. Lett.*, **103**(26), p. 263114.
- [55] Qin, Q., Yin, S., Cheng, G., Li, X., Chang, T.-H., Richter, G., Zhu, Y., and Gao, H., 2015, "Recoverable Plasticity in Penta-Twinned Metallic Nanowires Governed by Dislocation Nucleation and Retraction," *Nat. Commun.*, **6**, p. 5983.
- [56] Ramachandramoorthy, R., Gao, W., Bernal, R., and Espinosa, H., 2016, "High Strain Rate Tensile Testing of Silver Nanowires: Rate-Dependent Brittle-to-Ductile Transition," *Nano Lett.*, **16**(1), pp. 255–263.
- [57] Zhu, Y., Ke, C., and Espinosa, H. D., 2007, "Experimental Techniques for the Mechanical Characterization of One-Dimensional Nanostructures," *Exp. Mech.*, **47**, pp. 7–24.
- [58] Li, X. D., Chasiotis, I., and Kitamura, T., 2010, "In Situ Scanning Probe Microscopy Nanomechanical Testing," *MRS Bull.*, **35**(5), pp. 361–367.
- [59] Chen, Y., Dorgan, B. L., McIlroy, D. N., and Eric Aston, D., 2006, "On the Importance of Boundary Conditions on Nanomechanical Bending Behavior and Elastic Modulus Determination of Silver Nanowires," *J. Appl. Phys.*, **100**(10), p. 104301.
- [60] Jing, G. Y., Duan, H. L., Sun, X. M., Zhang, Z. S., Xu, J., Li, Y. D., Wang, J. X., and Yu, D. P., 2006, "Surface Effects on Elastic Properties of Silver Nanowires: Contact Atomic-Force Microscopy," *Phys. Rev. B*, **73**, p. 235409.
- [61] Qin, Q., Xu, F., Cao, Y., Ro, P. I., and Zhu, Y., 2012, "Measuring True Young's Modulus of a Cantilevered Nanowire: Effect of Clamping on Resonance Frequency," *Small*, **8**(16), pp. 2571–2576.
- [62] Murphy, K. F., Chen, L. Y., and Gianola, D. S., 2013, "Effect of Organometallic Clamp Properties on the Apparent Diversity of Tensile Response of Nanowires," *Nanotechnology*, **24**(23), p. 235704.
- [63] Zhang, H., Tang, J., Zhang, L., An, B., and Qin, L.-C., 2008, "Atomic Force Microscopy Measurement of the Young's Modulus and Hardness of Single LaB<sub>6</sub> Nanowires," *Appl. Phys. Lett.*, **92**(17), p. 173121.
- [64] Ni, H., and Li, X. D., 2006, "Young's Modulus of ZnO Nanobelts Measured Using Atomic Force Microscopy and Nanoindentation Techniques," *Nanotechnology*, **17**(14), pp. 3591–3597.
- [65] Ni, H., Li, X. D., and Gao, H. S., 2006, "Elastic Modulus of Amorphous SiO<sub>2</sub> Nanowires," *Appl. Phys. Lett.*, **88**(4), p. 043108.
- [66] Wong, E. W., Sheehan, P. E., and Lieber, C. M., 1997, "Nanobeam Mechanics: Elasticity, Strength, and Toughness of Nanorods and Nanotubes," *Science*, **277**(5334), pp. 1971–1975.
- [67] Heidelberg, A., Ngo, L. T., Wu, B., Phillips, M. A., Sharma, S., Kamins, T. I., Sader, J. E., and Boland, J. J., 2006, "A Generalized Description of the Elastic Properties of Nanowires," *Nano Lett.*, **6**(6), pp. 1101–1106.
- [68] Wen, B., Sader, J. E., and Boland, J. J., 2008, "Mechanical Properties of ZnO Nanowires," *Phys. Rev. Lett.*, **101**, p. 175502.
- [69] Ngo, L. T., Alméjida, D., Sader, J. E., Daly, B., Petkov, N., Holmes, J. D., Ertz, D., and Boland, J. J., 2006, "Ultimate-Strength Germanium Nanowires," *Nano Lett.*, **6**(12), pp. 2964–2968.
- [70] Lucas, M., Leach, A. M., McDowell, M. T., Hunyadi, S. E., Gall, K., Murphy, C. J., and Riedo, E., 2008, "Plastic Deformation of Pentagonal Silver Nanowires: Comparison Between AFM Nanoindentation and Atomistic Simulations," *Phys. Rev. B*, **77**, p. 245420.
- [71] Rabe, U., Janser, K., and Arnold, W., 1996, "Vibrations of Free and Surface-Coupled Atomic Force Microscope Cantilevers: Theory and Experiment," *Rev. Sci. Instrum.*, **67**(9), pp. 3281–3293.
- [72] Yamanaka, K., Maruyama, Y., Tsuji, T., and Nakamoto, K., 2001, "Resonance Frequency and Q Factor Mapping by Ultrasonic Atomic Force Microscopy," *Appl. Phys. Lett.*, **78**(13), pp. 1939–1941.
- [73] Hurley, D. C., Shen, K., Jennett, N. M., and Turner, J. A., 2003, "Atomic Force Acoustic Microscopy Methods to Determine Thin-Film Elastic Properties," *J. Appl. Phys.*, **94**(4), pp. 2347–2354.
- [74] Stan, G., King, S. W., and Cook, R. F., 2012, "Nanoscale Mapping of Contact Stiffness and Damping by Contact Resonance Atomic Force Microscopy," *Nanotechnology*, **23**(21), p. 215703.
- [75] Marszalek, P. E., Greenleaf, W. J., Li, H., Oberhauser, A. F., and Fernandez, J. M., 2000, "Atomic Force Microscopy Captures Quantized Plastic Deformation in Gold Nanowires," *Proc. Natl. Acad. Sci. U.S.A.*, **97**(12), pp. 6282–6286.
- [76] Marszalek, P. E., Li, H., Oberhauser, A. F., and Fernandez, J. M., 2002, "Chair-Boat Transitions in Single Polysaccharide Molecules Observed With Force-Ramp AFM," *Proc. Natl. Acad. Sci.*, **99**(7), pp. 4278–4283.
- [77] Rief, M., Gautel, M., Oesterhelt, F., Fernandez, J. M., and Gaub, H. E., 1997, "Reversible Unfolding of Individual Titin Immunoglobulin Domains by AFM," *Science*, **276**(5315), pp. 1109–1112.
- [78] Strus, M. C., Lahiji, R. R., Ares, P., López, V., Raman, A., and Reifengerger, R., 2009, "Strain Energy and Lateral Friction Force Distributions of Carbon Nanotubes Manipulated Into Shapes by Atomic Force Microscopy," *Nanotechnology*, **20**, p. 385709.
- [79] Stan, G., Krylyuk, S., Davydov, A. V., Levin, I., and Cook, R. F., 2012, "Ultimate Bending Strength of Si Nanowires," *Nano Lett.*, **12**(5), pp. 2599–2604.
- [80] Bordag, M., Ribayrol, A., Conache, G., Froberg, L. E., Gray, S., Samuelson, L., Montelius, L., and Pettersson, H., 2007, "Shear Stress Measurements on InAs Nanowires by AFM Manipulation," *Small*, **3**(8), pp. 1398–1401.
- [81] Qin, Q., and Zhu, Y., 2011, "Static Friction Between Silicon Nanowires and Elastomeric Substrates," *ACS Nano*, **5**(9), pp. 7404–7410.
- [82] Li, X., Gao, H., Murphy, C. J., and Gou, L., 2004, "Nanoindentation of Cu<sub>2</sub>O Nanocubes," *Nano Lett.*, **4**, pp. 1903–1907.
- [83] Mao, S. X., Zhao, M., and Wang, Z. L., 2003, "Nanoscale Mechanical Behavior of Individual Semiconducting Nanobelts," *Appl. Phys. Lett.*, **83**(5), pp. 993–995.
- [84] Li, X., Wang, X., Xiong, Q., and Eklund, P. C., 2005, "Mechanical Properties of ZnS Nanobelts," *Nano Lett.*, **5**(10), pp. 1982–1986.
- [85] Feng, G., Nix, W. D., Yoon, Y., and Lee, C. J., 2006, "A Study of the Mechanical Properties of Nanowires Using Nanoindentation," *J. Appl. Phys.*, **99**(7), p. 074304.
- [86] Shu, S. Q., Yang, Y., Fu, T., Wen, C. S., and Lu, J., 2009, "Can Young's Modulus and Hardness of Wire Structural Materials be Directly Measured Using Nanoindentation?," *J. Mater. Res.*, **24**(3), pp. 1054–1058.
- [87] Wu, X., Amin, S. S., and Xu, T. T., 2010, "Substrate Effect on the Young's Modulus Measurement of TiO<sub>2</sub> Nanoribbons by Nanoindentation," *J. Mater. Res.*, **25**(5), pp. 935–942.
- [88] Kim, Y.-J., Son, K., Choi, I.-C., Choi, I.-S., Park, W. II., and Jang, J., 2011, "Exploring Nanomechanical Behavior of Silicon Nanowires: AFM Bending Versus Nanoindentation," *Adv. Funct. Mater.*, **21**(20), pp. 279–286.
- [89] Ogletree, D. F., Carpick, R. W., and Salmeron, M., 1996, "Calibration of Frictional Forces in Atomic Force Microscopy," *Rev. Sci. Instrum.*, **67**(9), pp. 3298–3306.
- [90] Li, Q., Kim, K.-S., and Rydberg, A., 2006, "Lateral Force Calibration of an Atomic Force Microscope With a Diamagnetic Levitation Spring System," *Rev. Sci. Instrum.*, **77**(6), p. 65105.
- [91] Cannara, R. J., Eglin, M., and Carpick, R. W., 2006, "Lateral Force Calibration in Atomic Force Microscopy: A New Lateral Force Calibration Method and General Guidelines for Optimization," *Rev. Sci. Instrum.*, **77**(5), p. 53701.

- [92] Chen, C. Q., and Zhu, J., 2007, "Bending Strength and Flexibility of ZnO Nanowires," *Appl. Phys. Lett.*, **90**(4), p. 043105.
- [93] Hoffmann, S., Utke, I., Moser, B., Michler, J., Christiansen, S. H., Schmidt, V., Senz, S., Werner, P., Gosele, U., and Ballif, C., 2006, "Measurement of the Bending Strength of Vapor-Liquid-Solid Grown Silicon Nanowires," *Nano Lett.*, **6**(4), pp. 622–625.
- [94] Hoffmann, S., Ostlund, F., Michler, J., Fan, H. J., Zacharias, M., Christiansen, S. H., and Ballif, C., 2007, "Fracture Strength and Young's Modulus of ZnO Nanowires," *Nanotechnology*, **18**(20), p. 205503.
- [95] Xu, F., Qin, Q. Q., Mishra, A., Gu, Y., and Zhu, Y., 2010, "Mechanical Properties of ZnO Nanowires Under Different Loading Modes," *Nano Res.* **3**(4), pp. 271–280.
- [96] Lin, C.-H., Ni, H., Wang, X., Chang, M., Chao, Y. J., Deka, J. R., and Li, X., 2010, "In Situ Nanomechanical Characterization of Single-Crystalline Boron Nanowires by Buckling," *Small*, **6**(8), pp. 927–931.
- [97] Hsin, C.-L., Mai, W., Gu, Y., Gao, Y., Huang, C.-T., Liu, Y., Chen, L.-J., and Wang, Z.-L., 2008, "Elastic Properties and Buckling of Silicon Nanowires," *Adv. Mater.*, **20**(20), pp. 3919–3923.
- [98] Agrawal, R., Peng, B., Gdoutos, E., and Espinosa, H. D., 2008, "Elasticity Size Effects in ZnO Nanowires—A Combined Experimental-Computational Approach," *Nano Lett.*, **8**(11), pp. 3668–3674.
- [99] He, M.-R., Shi, Y., Zhou, W., Chen, J. W., Yan, Y. J., and Zhu, J., 2009, "Diameter Dependence of Modulus in Zinc Oxide Nanowires and the Effect of Loading Mode: In Situ Experiments and Universal Core-Shell Approach," *Appl. Phys. Lett.*, **95**(9), p. 91912.
- [100] Desai, A. V., and Haque, M. A., 2007, "Sliding of Zinc Oxide Nanowires on Silicon Substrate," *Appl. Phys. Lett.*, **90**(3), p. 33102.
- [101] Cheng, G., Miao, C., Qin, Q., Li, J., Xu, F., Haftbaradaran, H., Dickey, E. C., Gao, H., and Zhu, Y., 2015, "Large Anelasticity and Associated Energy Dissipation in Single-Crystalline Nanowires," *Nat. Nanotechnol.*, **10**, pp. 687–691.
- [102] Chang, T.-H., Cheng, G., Li, C., and Zhu, Y., 2016, "On the Size-Dependent Elasticity of Penta-Twinned Silver Nanowires," *Extrem. Mech. Lett.*, **8**, pp. 177–183.
- [103] Gianola, D. S., and Eberl, C., 2009, "Micro- and Nanoscale Tensile Testing of Materials," *JOM*, **61**, pp. 24–35.
- [104] Kiener, D., and Minor, A. M., 2011, "Source Truncation and Exhaustion: Insights From Quantitative In Situ TEM Tensile Testing," *Nano Lett.*, **11**(9), pp. 3816–3820.
- [105] Yu, Q., Qi, L., Chen, K., Mishra, R. K., Li, J., and Minor, A. M., 2012, "The Nanostructured Origin of Deformation Twinning," *Nano Lett.*, **12**(2), pp. 887–892.
- [106] Kiener, D., Grosinger, W., Dehm, G., and Pippan, R., 2008, "A Further Step Towards an Understanding of Size-Dependent Crystal Plasticity: In Situ Tension Experiments of Miniaturized Single-Crystal Copper Samples," *Acta Mater.*, **56**(3), pp. 580–592.
- [107] Wang, J., and Mao, S. X., 2016, "Atomistic Perspective on In Situ Nanomechanics Extrem," *Mech. Lett.*, **8**, pp. 127–139.
- [108] Wang, J., Zeng, Z., Weinberger, C. R., Zhang, Z., Zhu, T., and Mao, S. X., 2015, "In Situ Atomic-Scale Observation of Twinning-Dominated Deformation in Nanoscale Body-Centred Cubic Tungsten," *Nat. Mater.*, **14**, pp. 594–600.
- [109] Lu, Y., Huang, J. Y., Wang, C., Sun, S., and Lou, J., 2010, "Cold Welding of Ultrathin Gold Nanowires," *Nat. Nanotechnol.*, **5**, pp. 218–224.
- [110] Eberl, C., Gianola, D. S., and Thompson, R., 2006, "Digital Image Correlation and Tracking," File ID: 12413.
- [111] Ding, W., Calabri, L., Chen, X., Kohlhaas, K. M., and Ruoff, R. S., 2006, "Mechanics of Crystalline Boron Nanowires," *Compos. Sci. Technol.*, **66**(9), pp. 1112–1124.
- [112] Zhu, Y., 2016, "In-Situ Nanomechanical Testing of Crystalline Nanowires in Electron Microscopes," *JOM*, **68**(1), pp. 84–93.
- [113] Kahn, H., Ballarini, R., Mullen, R. L., and Heuer, A. H., 1999, "Electrostatically Actuated Failure of Microfabricated Polysilicon Fracture Mechanics Specimens," *Proc. R. Soc. London Ser. A*, **455**(1990), pp. 3807–3823.
- [114] Haque, M. A., and Saif, M. T. A., 2003, "A Review of MEMS-Based Microscale and Nanoscale Tensile and Bending Testing," *Exp. Mech.*, **43**(3), pp. 248–255.
- [115] Corigliano, A., De Masi, B., Frangi, A., Comi, C., Villa, A., and Marchi, M., 2004, "Mechanical Characterization of Polysilicon Through On-Chip Tensile Tests," *J. Microelectromech. Syst.*, **13**(2), pp. 200–219.
- [116] Hazra, S. S., Baker, M. S., Beuth, J. L., and de Boer, M. P., 2009, "Demonstration of an In Situ On-Chip Tensile Tester," *J. Micromech. Microeng.*, **19**, p. 082001.
- [117] Haque, M. A., Espinosa, H. D., and Lee, H. J., 2011, "MEMS for In Situ Testing—Handling, Actuation, Loading, and Displacement Measurements," *MRS Bull.*, **35**(5), pp. 375–381.
- [118] Zhu, Y., and Chang, T.-H., 2015, "A Review of Microelectromechanical Systems for Nanoscale Mechanical Characterization," *J. Micromech. Microeng.*, **25**(9), p. 93001.
- [119] Haque, M. A., and Saif, M. T. A., 2002, "In-Situ Tensile Testing of Nano-Scale Specimens in SEM and TEM," *Exp. Mech.*, **42**(1), pp. 123–128.
- [120] Haque, M. A., and Saif, M. T. A., 2002, "Application of MEMS Force Sensors for In Situ Mechanical Characterization of Nano-Scale Thin Films in SEM and TEM," *Sens. Actuators A* **97–98**, pp. 239–245.
- [121] Zhu, Y., Moldovan, N., and Espinosa, H. D., 2005, "A Microelectromechanical Load Sensor for In Situ Electron and X-Ray Microscopy Tensile Testing of Nanostructures," *Appl. Phys. Lett.*, **86**(1), p. 13506.
- [122] Zhu, Y., Corigliano, A., and Espinosa, H. D., 2006, "A Thermal Actuator for Nanoscale In Situ Microscopy Testing: Design and Characterization," *J. Micromech. Microeng.*, **16**(2), pp. 242–253.
- [123] Espinosa, H. D., Zhu, Y., and Moldovan, N., 2007, "Design and Operation of a MEMS-Based Material Testing System for Nanomechanical Characterization," *J. Microelectromech. Syst.*, **16**(5), pp. 1219–1231.
- [124] Hosseinian, E., and Pierron, O. N., 2013, "Quantitative In Situ TEM Tensile Fatigue Testing on Nanocrystalline Metallic Ultrathin Films," *Nanoscale*, **5**(24), pp. 12532–12541.
- [125] Chen, L. Y., Richter, G., Sullivan, J. P., and Gianola, D. S., 2012, "Lattice Anharmonicity in Defect-Free Pd Nanowhiskers," *Phys. Rev. Lett.*, **109**, p. 125503.
- [126] Zhang, D. F., Drissen, W., Breguet, J. M., Clavel, R., and Michler, J., 2009, "A High-Sensitivity and Quasi-Linear Capacitive Sensor for Nanomechanical Testing Applications," *J. Micromech. Microeng.*, **19**(7), p. 075003.
- [127] Steighner, M. S., Snedeker, L. P., Boyce, B. L., Gall, K., Miller, D. C., and Muhlstein, C. L., 2011, "Dependence on Diameter and Growth Direction of Apparent Strain to Failure of Si Nanowires," *J. Appl. Phys.*, **109**(3), p. 033503.
- [128] Ganesan, Y., Lu, Y., Peng, C., Ballarini, R., and Lou, J., 2010, "Development and Application of a Novel Microfabricated Device for the In Situ Tensile Testing of 1-D Nanomaterials," *J. Microelectromech. Syst.*, **19**(3), pp. 675–682.
- [129] Tsuchiya, T., Ura, Y., Sugano, K., and Tabata, O., 2012, "Electrostatic Tensile Testing Device With Nanonewton and Nanometer Resolution and Its Application to Nanowire Testing," *J. Microelectromech. Syst.*, **21**(3), pp. 523–529.
- [130] Yilmaz, M., and Kysar, J. W., 2013, "Monolithic Integration of Nanoscale Tensile Specimens and MEMS Structures," *Nanotechnology*, **24**(16), p. 165502.
- [131] Brown, J. J., Baca, A. I., Bertness, K. A., Dikin, D. A., Ruoff, R. S., and Bright, V. M., 2011, "Tensile Measurement of Single Crystal Gallium Nitride Nanowires on MEMS Test Stages," *Sens. Actuators, A*, **166**(2), pp. 177–186.
- [132] Zhang, Y., Liu, X., Ru, C., Zhang, Y. L., Dong, L., and Sun, Y., 2011, "Piezoresistivity Characterization of Synthetic Silicon Nanowires Using a MEMS Device," *J. Microelectromech. Syst.*, **20**(4), pp. 959–967.
- [133] Pant, B., Choi, S., Baumert, E. K., Allen, B. L., Graham, S., Gall, K., and Pierron, O. N., 2012, "MEMS-Based Nanomechanics: Influence of MEMS Design on Test Temperature," *Exp. Mech.*, **52**(6), pp. 607–617.
- [134] Chen, L. Y., Terrab, S., Murphy, K. F., Sullivan, J. P., Cheng, X., and Gianola, D. S., 2014, "Temperature Controlled Tensile Testing of Individual Nanowires," *Rev. Sci. Instrum.*, **85**(1), p. 13901.
- [135] Kang, W., and Saif, M. T. A., 2011, "A Novel SiC MEMS Apparatus for In Situ Uniaxial Testing of Micro/Nanomaterials at High Temperature," *J. Micromech. Microeng.*, **21**(10), p. 105017.
- [136] Bernal, R. A., Filleter, T., Connell, J., Sohn, K., Huang, J., Lauhon, L. J., and Espinosa, H. D., 2014, "In Situ Electron Microscopy Four-Point Electromechanical Characterization of Freestanding Metallic and Semiconducting Nanowires," *Small*, **10**(4), pp. 725–733.
- [137] Murphy, K. F., Piccione, B., Zanjani, M. B., Lukes, J. R., and Gianola, D. S., 2014, "Strain- and Defect-Mediated Thermal Conductivity in Silicon Nanowires," *Nano Lett.*, **14**(7), pp. 3785–3792.
- [138] Qin, Q., and Zhu, Y., 2013, "Temperature Control in Thermal Microactuators With Applications to In-Situ Nanomechanical Testing," *Appl. Phys. Lett.*, **102**(1), p. 13101.
- [139] Lu, S. N., Chung, J., and Ruoff, R. S., 2005, "Controlled Deposition of Nanotubes on Opposing Electrodes," *Nanotechnology*, **16**(9), pp. 1765–1770.
- [140] Guo, H., Chen, K., Oh, Y., Wang, K., Dejoie, C., Syed Asif, S. A., Warren, O. L., Shan, Z. W., Wu, J., and Minor, A. M., 2011, "Mechanics and Dynamics of the Strain-Induced M1-M2 Structural Phase Transition in Individual VO<sub>2</sub> Nanowires," *Nano Lett.*, **11**(8), pp. 3207–3213.
- [141] Naraghi, M., Chasiotis, I., Kahn, H., Wen, Y. K., and Dzenis, Y., 2007, "Mechanical Deformation and Failure of Electrospun Polyacrylonitrile Nanofibers as a Function of Strain Rate," *Appl. Phys. Lett.*, **91**(15), p. 151901.
- [142] Ganesan, Y., Peng, C., Lu, Y., Ci, L., Srivastava, A., Ajayan, P. M., and Lou, J., 2010, "Effect of Nitrogen Doping on the Mechanical Properties of Carbon Nanotubes," *ACS Nano*, **4**(12), pp. 7637–7643.
- [143] Espinosa, H. D., Bernal, R. A., and Filleter, T., 2012, "In Situ TEM Electromechanical Testing of Nanowires and Nanotubes," *Small*, **8**(21), pp. 3233–3252.
- [144] Song, J. H., Wang, X. D., Riedo, E., and Wang, Z. L., 2005, "Elastic Property of Vertically Aligned Nanowires," *Nano Lett.*, **5**(10), pp. 1954–1958.
- [145] Gordon, M. J., Baron, T., Dhalluin, F., Gentile, P., and Ferret, P., 2009, "Size Effects in Mechanical Deformation and Fracture of Cantilevered Silicon Nanowires," *Nano Lett.*, **9**(2), pp. 525–529.
- [146] Miller, R. E., and Shenoy, V. B., 2000, "Size-Dependent Elastic Properties of Nanosized Structural Elements," *Nanotechnology*, **11**(3), pp. 139–147.
- [147] Dingreville, R., Qu, J., and Cherkoum, M., 2005, "Surface Free Energy and Its Effect on the Elastic Behavior of Nano-Sized Particles, Wires and Films," *J. Mech. Phys. Solids*, **53**(8), pp. 1827–1854.
- [148] Diao, J. K., Gall, K., and Dunn, M. L., 2004, "Atomistic Simulation of the Structure and Elastic Properties of Gold Nanowires," *J. Mech. Phys. Solids*, **52**(9), pp. 1935–1962.
- [149] Zhou, L. G., and Huang, H. C., 2004, "Are Surfaces Elastically Softer or Stiffer?," *Appl. Phys. Lett.*, **84**(11), pp. 1940–1942.
- [150] Sharma, P., Ganti, S., and Bhate, N., 2003, "Effect of Surfaces on the Size-Dependent Elastic State of Nano-Inhomogeneities," *Appl. Phys. Lett.*, **82**(4), pp. 535–537.

- [151] Liang, H. Y., Upmanyu, M., and Huang, H. C., 2005, "Size-Dependent Elasticity of Nanowires: Nonlinear Effects," *Phys. Rev. B*, **71**, p. 241403.
- [152] McDowell, M. T., Leach, A. M., and Gall, K., 2008, "Bending and Tensile Deformation of Metallic Nanowires Model," *Simul. Mater. Sci. Eng.*, **16**(4), p. 45003.
- [153] Diao, J. K., Gall, K., and Dunn, M. L., 2003, "Surface-Stress-Induced Phase Transformation in Metal Nanowires," *Nat. Mater.*, **2**, pp. 656–660.
- [154] Shim, H. W., Zhou, L. G., Huang, H., and Cale, T. S., 2005, "Nanoplate Elasticity Under Surface Reconstruction," *Appl. Phys. Lett.*, **86**(15), p. 151912.
- [155] He, J., and Lilley, C. M., 2008, "Surface Effect on the Elastic Behavior of Static Bending Nanowires," *Nano Lett.*, **8**(7), pp. 1798–1802.
- [156] Song, F., Huang, G. L., Park, H. S., and Liu, X. N., 2011, "A Continuum Model for the Mechanical Behavior of Nanowires Including Surface and Surface-Induced Initial Stresses," *Int. J. Solids Struct.*, **48**(14–15), pp. 2154–2163.
- [157] Wang, G., and Feng, X., 2009, "Surface Effects on Buckling of Nanowires Under Uniaxial Compression," *Appl. Phys. Lett.*, **94**(14), p. 141913.
- [158] Park, H., and Klein, P., 2008, "Surface Stress Effects on the Resonant Properties of Metal Nanowires: The Importance of Finite Deformation Kinematics and the Impact of the Residual Surface Stress," *J. Mech. Phys. Solids*, **56**(11), pp. 3144–3166.
- [159] Yun, G., and Park, H., 2009, "Surface Stress Effects on the Bending Properties of fcc Metal Nanowires," *Phys. Rev. B*, **79**, p. 195421.
- [160] Wang, J., Huang, Z., Duan, H., Yu, S., Feng, X., Wang, G., Zhang, W., and Wang, T., 2011, "Surface Stress Effect in Mechanics of Nanostructured Materials," *Acta Mech. Solida Sin.*, **24**(1), pp. 52–82.
- [161] Lee, B., and Rudd, R. E., 2007, "First-Principles Calculation of Mechanical Properties of Si <001> Nanowires and Comparison to Nanomechanical Theory," *Phys. Rev. B*, **75**, p. 195328.
- [162] Tabib-Azar, M., Nassirou, M., Wang, R., Sharma, S., Kamins, T. I., Islam, M. S., and Williams, R. S., 2005, "Mechanical Properties of Self-Welded Silicon Nanobridges," *Appl. Phys. Lett.*, **87**(11), p. 113102.
- [163] Kang, K., and Cai, W., 2007, "Brittle and Ductile Fracture of Semiconductor Nanowires—Molecular Dynamics Simulations," *Philos. Mag.*, **87**(14–15), pp. 2169–2189.
- [164] Han, X., Zheng, K., Zhang, Y. F., Zhang, X., Zhang, Z., and Wang, Z. L., 2007, "Low-Temperature In Situ Large-Strain Plasticity of Silicon Nanowires," *Adv. Mater.*, **19**(16), pp. 2112–2118.
- [165] Li, X. X., Ono, T., Wang, Y. L., and Esashi, M., 2003, "Ultrathin Single-Crystalline-Silicon Cantilever Resonators: Fabrication Technology and Significant Specimen Size Effect on Young's Modulus," *Appl. Phys. Lett.*, **83**(15), pp. 3081–3083.
- [166] Desai, A. V., and Haque, M. A., 2007, "Mechanical Properties of ZnO Nanowires," *Sens. Actuators A*, **134**(1), pp. 169–176.
- [167] Bai, X. D., Gao, P. X., Wang, Z. L., and Wang, E. G., 2003, "Dual-Mode Mechanical Resonance of Individual ZnO Nanobelts," *Appl. Phys. Lett.*, **82**(26), pp. 4806–4808.
- [168] Zhu, Y., Qin, Q. Q., Xu, F., Fan, F. R., Ding, Y., Zhang, T., Wiley, B. J., and Wang, Z. L., 2012, "Size Effects on Elasticity, Yielding and Fracture of Silver Nanowires: In Situ Experiments," *Phys. Rev. B*, **85**, p. 45443.
- [169] Filleter, T., Ryu, S., Kang, K., Yin, J., Bernal, R. A., Sohn, K., Li, S., Huang, J., Cai, W., and Espinosa, H. D., 2012, "Nucleation-Controlled Distributed Plasticity in Penta-Twinned Silver Nanowires," *Small*, **8**(19), pp. 2986–2993.
- [170] Wu, B., Heidelberg, A., Boland, J. J., Sader, J. E., Sun, X., and Li, Y., 2006, "Microstructure-Hardened Silver Nanowires," *Nano Lett.*, **6**(3), pp. 468–472.
- [171] Alducin, D., Borja, R., Ortega, E., Velazquez-Salazar, J. J., Covarrubias, M., Santoyo, F. M., Bazán-Díaz, L., Sanchez, J. E., Torres, N., Ponce, A., and José-Yacamán, M., 2016, "In Situ Transmission Electron Microscopy Mechanical Deformation and Fracture of a Silver Nanowire," *Scr. Mater.*, **113**, pp. 63–67.
- [172] Park, H. S., 2008, "Surface Stress Effects on the Resonant Properties of Silicon Nanowires," *J. Appl. Phys.*, **103**(12), p. 123504.
- [173] Sun, C. Q., 2007, "Size Dependence of Nanostructures: Impact of Bond Order Deficiency," *Prog. Solid State Chem.*, **35**(1), pp. 1–159.
- [174] Zhang, L., and Huang, H., 2006, "Young's Moduli of ZnO Nanoplates: Ab Initio Determinations," *Appl. Phys. Lett.*, **89**(18), p. 183111.
- [175] Kulkarni, A. J., Zhou, M., and Ke, F. J., 2005, "Orientation and Size Dependence of the Elastic Properties of Zinc Oxide Nanobelts," *Nanotechnology*, **16**(12), pp. 2749–2756.
- [176] Cao, G., and Chen, X., 2007, "Analysis of Size-Dependent Elastic Properties of ZnO Nanofilms Using Atomistic Simulations," *Phys. Rev. B*, **76**, p. 165407.
- [177] Bernal, R. A., Agrawal, R., Peng, B., Bertness, K. A., Sanford, N. A., Davydov, A. V., and Espinosa, H. D., 2011, "Effect of Growth Orientation and Diameter on the Elasticity of GaN Nanowires. A Combined In Situ TEM and Atomistic Modeling Investigation," *Nano Lett.*, **11**(2), pp. 548–555.
- [178] Jang, D., Li, X., Gao, H., and Greer, J. R., 2012, "Deformation Mechanisms in Nanotwinned Metal Nanopillars," *Nat. Nanotechnol.*, **7**, pp. 594–601.
- [179] Seo, J.-H., Yoo, Y., Park, N.-Y., Yoon, S.-W., Lee, H., Han, S., Lee, S.-W., Seong, T.-Y., Lee, S.-C., Lee, K.-B., Cha, P.-R., Park, H. S., Kim, B., and Ahn, J.-P., 2011, "Superplastic Deformation of Defect-Free Au Nanowires Via Coherent Twin Propagation," *Nano Lett.*, **11**(8), pp. 3499–3502.
- [180] Wiley, B., Sun, Y., Mayers, B., and Xia, Y., 2005, "Shape-Controlled Synthesis of Metal Nanostructures: The Case of Silver," *Chem. Eur. J.*, **11**(2), pp. 454–463.
- [181] McDowell, M. T., Leach, A. M., and Gall, K., 2008, "On the Elastic Modulus of Metallic Nanowires," *Nano Lett.*, **8**(11), pp. 3613–3618.
- [182] Yoo, J. H., Oh, S. I., and Jeong, M. S., 2010, "The Enhanced Elastic Modulus of Nanowires Associated With Multitwins," *J. Appl. Phys.*, **107**(9), p. 94316.
- [183] Wu, J. Y., Nagao, S., He, J. Y., and Zhang, Z. L., 2011, "Role of Five-Fold Twin Boundary on the Enhanced Mechanical Properties of fcc Fe Nanowires," *Nano Lett.*, **11**(12), pp. 5264–5273.
- [184] Zheng, Y. G., Zhao, Y. T., Ye, H. F., and Zhang, H. W., 2014, "Size-Dependent Elastic Moduli and Vibrational Properties of Fivefold Twinned Copper Nanowires," *Nanotechnology*, **25**(31), p. 315701.
- [185] Wen, Y.-H., Huang, R., Zhu, Z.-Z., and Wang, Q., 2012, "Mechanical Properties of Platinum Nanowires: An Atomistic Investigation on Single-Crystalline and Twinned Structures," *Comput. Mater. Sci.*, **55**, pp. 205–210.
- [186] Niekiefel, F., Spiecker, E., and Bitzek, E., 2015, "Influence of Anisotropic Elasticity on the Mechanical Properties of Fivefold Twinned Nanowires," *J. Mech. Phys. Solids*, **84**, pp. 358–379.
- [187] Bernal, R. A., Aghaei, A., Lee, S., Ryu, S., Sohn, K., Huang, J., Cai, W., and Espinosa, H., 2015, "Intrinsic Bauschinger Effect and Recoverable Plasticity in Pentatwinned Silver Nanowires Tested in Tension," *Nano Lett.*, **15**(1), pp. 139–146.
- [188] Zheng, X.-P., Cao, Y.-P., Li, B., Feng, X.-Q., and Wang, G.-F., 2010, "Surface Effects in Various Bending-Based Test Methods for Measuring the Elastic Property of Nanowires," *Nanotechnology*, **21**(20), p. 205702.
- [189] Pearson, G., Read, W., and Feldmann, W., 1957, "Deformation and Fracture of Small Silicon Crystals," *Acta Metall.*, **5**(4), pp. 181–191.
- [190] Johansson, S., Schweitz, J.-Å., Tenerz, L., and Tiren, J., 1988, "Fracture Testing of Silicon Microelements In Situ in a Scanning Electron Microscope," *J. Appl. Phys.*, **63**(10), pp. 4799–4803.
- [191] Nakao, S., Ando, T., Shikida, M., and Satoh, K., 2006, "Mechanical Properties of a Micron-Sized SCS Film in a High-Temperature Environment," *J. Micro-mech. Microeng.*, **16**(4), pp. 715–720.
- [192] Zhang, D., Breguet, J.-M., Clavel, R., Sivakov, V., Christiansen, S., and Michler, J., 2010, "In Situ Electron Microscopy Mechanical Testing of Silicon Nanowires Using Electrostatically Actuated Tensile Stages," *J. Microelectromech. Syst.*, **19**(3), pp. 663–674.
- [193] Tang, D.-M., Ren, C.-L., Wang, M.-S., Wei, X., Kawamoto, N., Liu, C., Bando, Y., Mitome, M., Fukata, N., and Golberg, D., 2012, "Mechanical Properties of Si Nanowires as Revealed by In Situ Transmission Electron Microscopy and Molecular Dynamics Simulations," *Nano Lett.*, **12**(4), pp. 1898–1904.
- [194] Wagner, A., Hintsala, E., Kumar, P., Gerberich, W., and Mkhoyan, K., 2015, "Mechanisms of Plasticity in Near-Theoretical Strength Sub-100 nm Si Nanocubes," *Acta Mater.*, **100**, pp. 256–265.
- [195] Agrawal, R., Peng, B., and Espinosa, H. D., 2009, "Strength and Fracture Mechanism of Zinc Oxide Nanowires Under Uniaxial Tensile Load," *Nano Lett.*, **9**(12), pp. 4177–4183.
- [196] Cheng, G., Chang, T.-H., Qin, Q., Huang, H., and Zhu, Y., 2014, "Mechanical Properties of Silicon Carbide Nanowires: Effect of Size-Dependent Defect Density," *Nano Lett.*, **14**(2), pp. 754–758.
- [197] Narayanan, S., Cheng, G., Zeng, Z., Zhu, Y., and Zhu, T., 2015, "Strain Hardening and Size Effect in Five-Fold Twinned Ag Nanowires," *Nano Lett.*, **15**(6), pp. 4037–4044.
- [198] Brenner, S. S., 1956, "Tensile Strength of Whiskers," *J. Appl. Phys.*, **27**, pp. 1484–1491.
- [199] Tsuchiya, T., Hirata, M., Chiba, N., Udo, R., Yoshitomi, Y., Ando, T., Sato, K., Takashima, K., Higo, Y., Saotome, Y., Ogawa, H., and Ozaki, K., 2005, "Cross Comparison of Thin-Film Tensile-Testing Methods Examined Using Single-Crystal Silicon, Polysilicon, Nickel, and Titanium Films," *J. Microelectromech. Syst.*, **14**(5), pp. 1178–1186.
- [200] DelRio, F. W., Cook, R. F., and Boyce, B. L., 2015, "Fracture Strength of Micro- and Nano-Scale Silicon Components," *Appl. Phys. Rev.*, **2**(2), p. 21303.
- [201] Sharpe, W. N., Jackson, K. M., Hemker, K. J., and Xie, Z. L., 2001, "Effect of Specimen Size on Young's Modulus and Fracture Strength of Polysilicon," *J. Microelectromech. Syst.*, **10**(3), pp. 317–326.
- [202] Boyce, B. L., Graziop, J. M., Buchheit, T. E., and Shaw, M. J., 2007, "Strength Distributions in Polycrystalline Silicon MEMS," *J. Microelectromech. Syst.*, **16**(2), pp. 179–190.
- [203] Ballarini, R., Kahn, H., Tayebi, N., and Heuer, A. H., 2000, "Effects of Microstructure on the Strength and Fracture Toughness of Polysilicon: A Wafer Level Testing Approach," Symposium on Mechanical Properties of Structural Films, C. L. Muhlstein, ed., American Society Testing and Materials, Orlando, FL, p. 37.
- [204] Chasiotis, I., and Knauss, W. G., 2003, "The Mechanical Strength of Polysilicon Films: Part 1. The Influence of Fabrication Governed Surface Conditions," *J. Mech. Phys. Solids*, **51**(8), pp. 1533–1550.
- [205] Soudi, A., Khan, E. H., Dickinson, J. T., and Gu, Y., 2009, "Observation of Unintentionally Incorporated Nitrogen-Related Complexes in ZnO and GaN Nanowires," *Nano Lett.*, **9**(5), pp. 1844–1849.
- [206] Agrawal, R., Bernal, R. A., Isheim, D., and Espinosa, H. D., 2011, "Characterizing Atomic Composition and Dopant Distribution in Wide Band Gap Semiconductor Nanowires Using Laser-Assisted Atom Probe Tomography," *J. Phys. Chem. C*, **115**(36), pp. 17688–17694.
- [207] Perea, D. E., Hemesath, E. R., Schwalbach, E. J., Lensch-Falk, J. L., Voores, P. W., and Lathon, L. J., 2009, "Direct Measurement of Dopant Distribution in an Individual Vapour-Liquid-Solid Nanowire," *Nat. Nanotechnol.*, **4**, pp. 315–319.
- [208] Lopez, F. J., Hemesath, E. R., and Lathon, L. J., 2009, "Ordered Stacking Fault Arrays in Silicon Nanowires," *Nano Lett.*, **9**(7), pp. 2774–2779.
- [209] He, M. R., and Zhu, J., 2011, "Defect-Dominated Diameter Dependence of Fracture Strength in Single-Crystalline ZnO Nanowires: In Situ Experiments," *Phys. Rev. B*, **83**, p. 161302.

- [210] He, M.-R., Xiao, P., Zhao, J., Dai, S., Ke, F., and Zhu, J., 2011, "Quantifying the Defect-Dominated Size Effect of Fracture Strain in Single Crystalline ZnO Nanowires," *J. Appl. Phys.*, **109**(12), p. 123504.
- [211] Kelly, T. F., and Miller, M. K., 2007, "Invited Review Article: Atom Probe Tomography," *Rev. Sci. Instrum.*, **78**(3), p. 031101.
- [212] Robertson, I. M., Schuh, C. A., Vetrano, J. S., Browning, N. D., Field, D. P., Jensen, D. J., Miller, M. K., Baker, I., Dunand, D. C., Dunin-Borkowski, R., Kabius, B., Kelly, T., Lozano-Perez, S., Misra, A., Rohrer, G. S., Rollett, A. D., Taheri, M. L., Thompson, G. B., Uchic, M., Wang, X.-L., and Was, G., 2011, "Towards an Integrated Materials Characterization Toolbox," *J. Mater. Res.*, **26**(11), pp. 1341–1383.
- [213] Shim, H. W., and Huang, H. C., 2007, "Three-Stage Transition During Silicon Carbide Nanowire Growth," *Appl. Phys. Lett.*, **90**(8), p. 083106.
- [214] Zhang, Y. F., Han, X. D., Zheng, K., Zhang, Z., Zhang, X. N., Fu, J. Y., Ji, Y., Hao, Y. J., Guo, X. Y., and Wang, Z. L., 2007, "Direct Observation of Super-Plasticity of Beta-SiC Nanowires at Low Temperature," *Adv. Funct. Mater.*, **17**(17), pp. 3435–3440.
- [215] Wang, J., Lu, C., Wang, Q., Xiao, P., Ke, F., Bai, Y., Shen, Y., Liao, X., and Gao, H., 2012, "Influence of Microstructures on Mechanical Behaviours of SiC Nanowires: A Molecular Dynamics Study," *Nanotechnology*, **23**(2), p. 25703.
- [216] Wu, Z., Zhang, Y.-W., Jhon, M. H., Gao, H., and Srolovitz, D. J., 2012, "Nanowire Failure: Long = Brittle and Short = Ductile," *Nano Lett.*, **12**(2), pp. 910–914.
- [217] Peng, C., Zhan, Y., and Lou, J., 2012, "Size-Dependent Fracture Mode Transition in Copper Nanowires," *Small*, **8**(12), pp. 1889–1894.
- [218] Chen, L. Y., He, M.-R., Shin, J., Richter, G., and Gianola, D. S., 2015, "Measuring Surface Dislocation Nucleation in Defect-Scarce Nanostructures," *Nat. Mater.*, **14**, pp. 707–713.
- [219] Liang, W., Zhou, M., and Ke, F., 2005, "Shape Memory Effect in Cu Nanowires," *Nano Lett.*, **5**(10), pp. 2039–2043.
- [220] Sedlmayr, A., Bitzek, E., Gianola, D. S., Richter, G., Mönig, R., and Kraft, O., 2012, "Existence of Two Twinning-Mediated Plastic Deformation Modes in Au Nanowhiskers," *Acta Mater.*, **60**(9), pp. 3985–3993.
- [221] Lu, K., Lu, L., and Suresh, S., 2009, "Strengthening Materials by Engineering Coherent Internal Boundaries at the Nanoscale," *Science*, **324**(5925), pp. 349–352.
- [222] Li, X., Wei, Y., Lu, L., Lu, K., and Gao, H., 2010, "Dislocation Nucleation Governed Softening and Maximum Strength in Nano-Twinned Metals," *Nature* **464**, pp. 877–880.
- [223] Sansoz, F., Huang, H., and Warner, D. H., 2008, "An Atomistic Perspective on Twinning Phenomena in Nano-Enhanced fcc Metals," *JOM*, **60**, pp. 79–84.
- [224] Deng, C., and Sansoz, F., 2009, "Enabling Ultrahigh Plastic Flow and Work Hardening in Twinned Gold Nanowires," *Nano Lett.*, **9**(4), pp. 1517–1522.
- [225] Wang, J., Sansoz, F., Huang, J., Liu, Y., Sun, S., Zhang, Z., and Mao, S. X., 2013, "Near-Ideal Theoretical Strength in Gold Nanowires Containing Angstrom Scale Twins," *Nat. Commun.*, **4**, p. 1742.
- [226] Rajagopalan, J., Han, J. H., and Saif, M. T. A., 2007, "Plastic Deformation Recovery in Freestanding Nanocrystalline Aluminum and Gold Thin Films," *Science*, **315**(5820), pp. 1831–1834.
- [227] Rajagopalan, J., Rentenberger, C., Peter Karnthaler, H., Dehm, G., and Saif, M. T. A., 2010, "In Situ TEM Study of Microplasticity and Bauschinger Effect in Nanocrystalline Metals," *Acta Mater.*, **58**(14), pp. 4772–4782.
- [228] Mompou, F., Caillard, D., Legros, M., and Mughrabi, H., 2012, "In Situ TEM Observations of Reverse Dislocation Motion Upon Unloading in Tensile-Deformed UFG Aluminium," *Acta Mater.*, **60**(8), pp. 3402–3414.
- [229] Xiang, Y., and Vlassak, J. J., 2005, "Bauschinger Effect in Thin Metal Films," *Scr. Mater.*, **53**(2), pp. 177–182.
- [230] Jennings, A. T., Gross, C., Greer, F., Aitken, Z. H., Lee, S.-W., Weinberger, C. R., and Greer, J. R., 2012, "Higher Compressive Strengths and the Bauschinger Effect in Conformally Passivated Copper Nanopillars," *Acta Mater.*, **60**(8), p. 3444.
- [231] Lee, S., Im, J., Yoo, Y., Bitzek, E., Kiener, D., Richter, G., Kim, B., and Oh, S. H., 2014, "Reversible Cyclic Deformation Mechanism of Gold Nanowires by Twinning-Detwinning Transition Evidenced From In Situ TEM," *Nat. Commun.*, **5**, p. 3033.
- [232] Sun, J., He, L., Lo, Y.-C., Xu, T., Bi, H., Sun, L., Zhang, Z., Mao, S. X., and Li, J., 2014, "Liquid-Like Pseudoelasticity of Sub-10-nm Crystalline Silver Particles," *Nat. Mater.*, **13**, pp. 1007–1012.
- [233] Schuh, C. A., Mason, J. K., and Lund, A. C., 2005, "Quantitative Insight Into Dislocation Nucleation From High-Temperature Nanoindentation Experiments," *Nat. Mater.*, **4**, pp. 617–621.
- [234] Li, J., 2015, "Dislocation Nucleation: Diffusive Origins," *Nat. Mater.*, **14**, pp. 656–657.
- [235] Lakes, R., 2009, *Viscoelastic Material*, Cambridge University Press, Cambridge, UK.
- [236] Zener, C., 1948, *Elasticity and Anelasticity of Metals*, University of Chicago Press, Chicago, IL.
- [237] Nowick, A. S., and Berry, B. S., 1972, *Anelastic Relaxation in Crystalline Solids*, Academic Press, New York.
- [238] Schaumann, G., Vökl, J., and Alefeld, G., 1968, "Relaxation Process Due to Long-Range Diffusion of Hydrogen and Deuterium in Niobium," *Phys. Rev. Lett.*, **21**, pp. 891–893.
- [239] Chen, B., Gao, Q., Wang, Y., Liao, X., Mai, Y.-W., Tan, H. H., Zou, J., Ringer, S. P., and Jagadish, C., 2013, "Anelastic Behavior in GaAs Semiconductor Nanowires," *Nano Lett.*, **13**(7), pp. 3169–3172.
- [240] Sheng, H., Zheng, H., Cao, F., Wu, S., Li, L., Liu, C., Zhao, D., and Wang, J., 2015, "Anelasticity of Twinned CuO Nanowires," *Nano Res.*, **8**(11), pp. 3687–3693.
- [241] Fan, Z. Y., Ho, J. C., Takahashi, T., Yerushalmi, R., Takei, K., Ford, A. C., Chueh, Y. L., and Javey, A., 2009, "Toward the Development of Printable Nanowire Electronics and Sensors," *Adv. Mater.*, **21**(37), pp. 3730–3743.
- [242] Ju, S., Facchetti, A., Xuan, Y., Liu, J., Ishikawa, F., Ye, P., Zhou, C., Marks, T. J., and James, D. B., 2007, "Fabrication of Fully Transparent Nanowire Transistors for Transparent and Flexible Electronics," *Nat. Nanotechnol.*, **2**, pp. 378–384.
- [243] McAlpine, M. C., Ahmad, H., Wang, D. W., and Heath, J. R., 2007, "Highly Ordered Nanowire Arrays on Plastic Substrates for Ultrasensitive Flexible Chemical Sensors," *Nat. Mater.*, **6**, pp. 379–384.
- [244] Lu, W., and Lieber, C. M., 2006, "Semiconductor Nanowires," *J. Phys. D: Appl. Phys.*, **39**, pp. R387–R406.
- [245] Xu, F., Lu, W., and Zhu, Y., 2011, "Controlled 3D Buckling of Silicon Nanowires for Stretchable Electronics," *ACS Nano*, **5**(1), pp. 672–678.
- [246] Yao, S., and Zhu, Y., 2014, "Wearable Multifunctional Sensors Using Printed Stretchable Conductors Made of Silver Nanowires," *Nanoscale*, **6**, pp. 2345–2352.
- [247] Meyyappan, M., and Sunkara, M. K., 2010, *Inorganic Nanowires: Applications, Properties and Characterization*, CRC Press, Boca Raton, FL.
- [248] Zhou, J., Gu, Y., Fei, P., Mai, W., Gao, Y., Yang, R., Bao, G., and Wang, Z. L., 2008, "Flexible Piezotronic Strain Sensor," *Nano Lett.*, **8**(9), pp. 3035–3040.
- [249] Hu, L. B., Kim, H. S., Lee, J. Y., Peumans, P., and Cui, Y., 2010, "Scalable Coating and Properties of Transparent, Flexible, Silver Nanowire Electrodes," *ACS Nano*, **4**(5), pp. 2955–2963.
- [250] Wu, J., Zang, J., Rathmell, A. R., Zhao, X., and Wiley, B. J., 2013, "Reversible Sliding in Networks of Nanowires," *Nano Lett.*, **13**(6), pp. 2381–2386.
- [251] Scardaci, V., Coull, R., Lyons, P. E., Rickard, D., and Coleman, J. N., 2011, "Spray Deposition of Highly Transparent, Low-Resistance Networks of Silver Nanowires Over Large Areas," *Small*, **7**(18), pp. 2621–2628.
- [252] Yu, Z., Zhang, Q., Li, L., Chen, Q., Niu, X., Liu, J., and Pei, Q., 2011, "Highly Flexible Silver Nanowire Electrodes for Shape-Memory Polymer Light-Emitting Diodes," *Adv. Mater.*, **23**(5), pp. 664–668.
- [253] Rogers, J. A., Someya, T., and Huang, Y. G., 2010, "Materials and Mechanics for Stretchable Electronics," *Science*, **327**(5973), pp. 1603–1607.
- [254] Khang, D. Y., Jiang, H. Q., Huang, Y., and Rogers, J. A., 2006, "A Stretchable Form of Single-Crystal Silicon for High-Performance Electronics on Rubber Substrates," *Science*, **311**(5758), pp. 208–212.
- [255] Kim, D.-H., Lu, N., Ma, R., Kim, Y.-S., Kim, R.-H., Wang, S., Wu, J., Won, S. M., Tao, H., Islam, A., Yu, K. J., Kim, T., Chowdhury, R., Ying, M., Xu, L., Li, M., Chung, H.-J., Keum, H., McCormick, M., Liu, P., Zhang, Y.-W., Omenetto, F. G., Huang, Y., Coleman, T., and Rogers, J. A., 2011, "Epidermal Electronics," *Science*, **333**(6044), pp. 838–843.
- [256] Kim, D., Xiao, J., Song, J., Huang, Y., and Rogers, J. A., 2010, "Stretchable, Curvilinear Electronics Based on Inorganic Materials," *Adv. Mater.*, **22**(19), pp. 2108–2124.
- [257] Hammock, M. L., Chortos, A., Tee, B. C.-K., Tok, J. B.-H., and Bao, Z., 2013, "25th Anniversary Article: The Evolution of Electronic Skin (E-Skin): A Brief History, Design Considerations, and Recent Progress," *Adv. Mater.*, **25**(42), pp. 5997–6038.
- [258] Ryu, S. Y., Xiao, J. L., Il Park, W., Son, K. S., Huang, Y. Y., Paik, U., and Rogers, J. A., 2009, "Lateral Buckling Mechanics in Silicon Nanowires on Elastomeric Substrates," *Nano Lett.*, **9**(9), pp. 3214–3219.
- [259] Durham, J. W., and Zhu, Y., 2013, "Fabrication of Functional Nanowire Devices on Unconventional Substrates Using Strain-Release Assembly," *ACS Appl. Mater. Interfaces*, **5**(2), pp. 256–261.
- [260] Hu, W., Niu, X., Li, L., Yun, S., Yu, Z., and Pei, Q., 2012, "Intrinsically Stretchable Transparent Electrodes Based on Silver-Nanowire-Crosslinked-Polyacrylate Composites," *Nanotechnology*, **23**(34), p. 344002.
- [261] Yao, S., and Zhu, Y., 2016, "Nanomaterial-Enabled Dry Electrodes for Electrophysiological Sensing: A Review," *JOM*, **68**(4), pp. 1145–1155.
- [262] Myers, A. C., Huang, H., and Zhu, Y., 2015, "Wearable Silver Nanowire Dry Electrodes for Electrophysiological Sensing," *RSC Adv.*, **5**(15), pp. 11627–11632.
- [263] Cui, Z., Poblete, F. R., Cheng, G., Yao, S., Jiang, X., and Zhu, Y., 2015, "Design and Operation of Silver Nanowire Based Flexible and Stretchable Touch Sensors," *J. Mater. Res.*, **30**(1), pp. 79–85.
- [264] Song, L., Myers, A. C., Adams, J. J., and Zhu, Y., 2014, "Stretchable and Reversibly Deformable Radio Frequency Antennas Based on Silver Nanowires," *ACS Appl. Mater. Interfaces*, **6**(6), pp. 4248–4253.
- [265] Chen, Y., Zhu, Y., Chen, X., and Liu, Y., 2016, "Mechanism of the Transition From In-Plane Buckling to Helical Buckling for a Stiff Nanowire on an Elastomeric Substrate," *ASME J. Appl. Mech.*, **83**(4), p. 041011.
- [266] Chen, Y., Liu, Y., Yan, Y., Zhu, Y., and Chen, X., 2016, "Helical Coil Buckling Mechanism for a Stiff Nanowire on an Elastomeric Substrate," *J. Mech. Phys. Solids*, **95**, pp. 25–43.
- [267] Jiang, T., Huang, R., and Zhu, Y., 2014, "Interfacial Sliding and Buckling of Monolayer Graphene on a Stretchable Substrate," *Adv. Funct. Mater.*, **24**(3), pp. 396–402.
- [268] Guo, G., and Zhu, Y., 2015, "Cohesive-Shear-Lag Modeling of Interfacial Stress Transfer Between a Monolayer Graphene and a Polymer Substrate," *ASME J. Appl. Mech.*, **82**(3), p. 031005.
- [269] Hwang, B., Kim, T., and Han, S. M., 2016, "Compression and Tension Bending Fatigue Behavior of Ag Nanowire Network Extrem," *Mech. Lett.*, **8**, pp. 266–272.
- [270] De Volder, M. F. L., Tawfik, S. H., Baughman, R. H., and Hart, A. J., 2013, "Carbon Nanotubes: Present and Future Commercial Applications," *Science*, **339**(6119), pp. 535–539.
- [271] Wu, R., Zhou, K., Yue, C. Y., Wei, J., and Pan, Y., 2015, "Recent Progress in Synthesis, Properties and Potential Applications of SiC Nanomaterials," *Prog. Mater. Sci.*, **72**, pp. 1–60.

- [272] Yang, W., Araki, H., Tang, C., Thaveethavorn, S., Kohyama, A., Suzuki, H., and Noda, T., 2005, "Single-Crystal SiC Nanowires With a Thin Carbon Coating for Stronger and Tougher Ceramic Composites," *Adv. Mater.*, **17**(12), pp. 1519–1523.
- [273] Yang, W., Araki, H., Kohyama, A., Yang, Q., Xu, Y., Yu, J., and Noda, T., 2007, "The Effect of SiC Nanowires on the Flexural Properties of CVI-SiC/SiC Composites," *J. Nucl. Mater.*, **367–370**(Pt. a), pp. 708–712.
- [274] Vivekchand, S. R. C., Ramamurty, U., and Rao, C. N. R., 2006, "Mechanical Properties of Inorganic Nanowire Reinforced Polymer–Matrix Composites," *Nanotechnology*, **17**(11), pp. S344–S350.
- [275] Yanhui, C., Qiangang, F., Hejun, L., Xiaohong, S., Kezhi, L., Xue, W., and Gunan, S., 2012, "Effect of SiC Nanowires on the Mechanical and Oxidation Protective Ability of SiC Coating for C/C Composites," *J. Am. Ceram. Soc.*, **95**(2), pp. 739–745.
- [276] Fu, Q.-G., Jia, B.-L., Li, H.-J., Li, K.-Z., and Chu, Y.-H., 2012, "SiC Nanowires Reinforced MAS Joint of SiC Coated Carbon/Carbon Composites to LAS Glass Ceramics," *Mater. Sci. Eng. A*, **532**, pp. 255–259.
- [277] Qian, D., Dickey, E. C., Andrews, R., and Rantell, T., 2000, "Load Transfer and Deformation Mechanisms in Carbon Nanotube-Polystyrene Composites," *Appl. Phys. Lett.*, **76**(20), pp. 2868–2870.
- [278] Thostenson, E. T., Ren, Z., and Chou, T.-W., 2001, "Advances in the Science and Technology of Carbon Nanotubes and Their Composites: A Review," *Compos. Sci. Technol.*, **61**(13), pp. 1899–1912.
- [279] Gao, X.-L., and Li, K., 2005, "A Shear-lag Model for Carbon Nanotube-Reinforced Polymer Composites," *Int. J. Solids Struct.*, **42**(5–6), pp. 1649–1667.
- [280] Chen, X., Zhang, L., Zheng, M., Park, C., Wang, X., and Ke, C., 2015, "Quantitative Nanomechanical Characterization of the van der Waals Interfaces Between Carbon Nanotubes and Epoxy," *Carbon*, **82**, pp. 214–228.
- [281] Wagner, H. D., and Vaia, R. A., 2004, "Nanocomposites: Issues at the Interface," *Mater. Today*, **7**(11), pp. 38–42.
- [282] Ding, W., Eitan, A., Fisher, F. T., Chen, X., Dikin, D. A., Andrews, R., Brinson, L. C., Schadler, L. S., and Ruoff, R. S., 2003, "Direct Observation of Polymer Sheathing in Carbon Nanotube-Polycarbonate Composites," *Nano Lett.*, **3**(11), pp. 1593–1597.
- [283] Loh, O., and Espinosa, H. D., 2012, "Nanoelectromechanical Contact Switches," *Nat. Nanotechnol.*, **7**, pp. 283–295.
- [284] Eom, K., Park, H. S., Yoon, D. S., and Kwon, T., 2011, "Nanomechanical Resonators and Their Applications in Biological/Chemical Detection: Nanomechanics Principles," *Phys. Rep.-Rev. Sect. Phys., Lett.*, **503**(4–5), pp. 115–163.
- [285] Han, J.-W., Ahn, J.-H., Kim, M.-W., Lee, J. O., Yoon, J.-B., and Choi, Y.-K., 2010, "Nanowire Mechanical Switch With a Built-In Diode," *Small*, **6**(11), pp. 1197–1200.
- [286] Li, Q., Koo, S.-M., Edelstein, M. D., Suehle, J. S., and Richter, C. A., 2007, "Silicon Nanowire Electromechanical Switches for Logic Device Application," *Nanotechnology*, **18**(31), p. 315202.
- [287] Feng, X. L., Matheny, M. H., Zorman, C. A., Mehregany, M., and Roukes, M. L., 2010, "Low Voltage Nanoelectromechanical Switches Based on Silicon Carbide Nanowires," *Nano Lett.*, **10**(8), pp. 2891–2896.
- [288] Husain, A., Hone, J., Postma, H. W. C., Huang, X. M. H., Drake, T., Barbic, M., Scherer, A., and Roukes, M. L., 2003, "Nanowire-Based Very-High-Frequency Electromechanical Resonator," *Appl. Phys. Lett.*, **83**(6), pp. 1240–1242.
- [289] Feng, X. L., He, R., Yang, P., and Roukes, M. L., 2007, "Very High Frequency Silicon Nanowire Electromechanical Resonators," *Nano Lett.*, **7**(7), pp. 1953–1959.
- [290] Li, M., Bhiladvala, R. B., Morrow, T. J., Sioss, J. A., Lew, K.-K., Redwing, J. M., Keating, C. D., and Mayer, T. S., 2008, "Bottom-Up Assembly of Large-Area Nanowire Resonator Arrays," *Nat. Nanotechnol.*, **3**, pp. 88–92.
- [291] Huang, Y., Bai, X., and Zhang, Y., 2006, "In Situ Mechanical Properties of Individual ZnO Nanowires and the Mass Measurement of Nanoparticles," *J. Phys. Condens. Matter*, **18**, pp. L179–L184.
- [292] Yang, Y. T., Callegari, C., Feng, X. L., Ekinic, K. L., and Roukes, M. L., 2006, "Zeptogram-Scale Nanomechanical Mass Sensing," *Nano Lett.*, **6**(4), pp. 583–586.
- [293] He, R., Feng, X. L., Roukes, M. L., and Yang, P. D., 2008, "Self-Transducing Silicon Nanowire Electromechanical Systems at Room Temperature," *Nano Lett.*, **8**(6), pp. 1756–1761.
- [294] Lou, L., Zhang, S., Park, W.-T., Tsai, J. M., Kwong, D.-L., and Lee, C., 2012, "Optimization of NEMS Pressure Sensors With a Multilayered Diaphragm Using Silicon Nanowires as Piezoresistive Sensing Elements," *J. Micromech. Microeng.*, **22**(5), p. 55012.
- [295] He, R. R., and Yang, P. D., 2006, "Giant Piezoresistance Effect in Silicon Nanowires," *Nat. Nanotechnol.*, **1**, pp. 42–46.
- [296] Kanda, Y., 1991, "Piezoresistance Effect of Silicon," *Sens. Actuators A*, **28**(2), pp. 83–91.
- [297] Rowe, A. C. H., 2014, "Piezoresistance in Silicon and Its Nanostructures," *J. Mater. Res.*, **29**(6), pp. 731–744.
- [298] Boukai, A. I., Bunimovich, Y., Tahir-Kheli, J., Yu, J. K., Goddard, W. A., and Heath, J. R., 2008, "Silicon Nanowires as Efficient Thermoelectric Materials," *Nature*, **451**, pp. 168–171.
- [299] Chen, J., Yang, J., Li, Z., Fan, X., Zi, Y., Jing, Q., Guo, H., Wen, Z., Pradel, K. C., Niu, S., and Wang, Z. L., 2015, "Networks of Triboelectric Nanogenerators for Harvesting Water Wave Energy: A Potential Approach Toward Blue Energy," *ACS Nano*, **9**(3), pp. 3324–3331.
- [300] Fan, F.-R., Tian, Z.-Q., and Lin Wang, Z., 2012, "Flexible Triboelectric Generator," *Nano Energy*, **1**(2), pp. 328–334.
- [301] Xu, S., Qin, Y., Xu, C., Wei, Y., Yang, R., and Wang, Z. L., 2010, "Self-Powered Nanowire Devices," *Nat. Nanotechnol.*, **5**, pp. 366–373.
- [302] Agrawal, R., and Espinosa, H. D., 2011, "Giant Piezoelectric Size Effects in Zinc Oxide and Gallium Nitride Nanowires. A First Principles Investigation," *Nano Lett.*, **11**(2), pp. 786–790.
- [303] Dai, S., Gharbi, M., Sharma, P., and Park, H. S., 2011, "Surface Piezoelectricity: Size Effects in Nanostructures and the Emergence of Piezoelectricity in Non-Piezoelectric Materials," *J. Appl. Phys.*, **110**(10), p. 104305.
- [304] Yan, Z., and Jiang, L. Y., 2011, "The Vibrational and Buckling Behaviors of Piezoelectric Nanobeams With Surface Effects," *Nanotechnology*, **22**(24), p. 245703.
- [305] Wang, G.-F., and Feng, X.-Q., 2010, "Effect of Surface Stresses on the Vibration and Buckling of Piezoelectric Nanowires," *EPL (Europhys. Lett.)*, **91**(5), p. 56007.
- [306] Boukamp, B. A., Lesh, G. C., and Huggins, R. A., 1981, "All-Solid Lithium Electrodes With Mixed-Conductor Matrix," *J. Electrochem. Soc.*, **128**(4), pp. 725–729.
- [307] Huang, J. Y., Zhong, L., Wang, C. M., Sullivan, J. P., Xu, W., Zhang, L. Q., Mao, S. X., Hudak, N. S., Liu, X. H., Subramanian, A., Fan, H., Qi, L., Kushima, A., and Li, J., 2010, "In Situ Observation of the Electrochemical Lithiation of a Single SnO<sub>2</sub> Nanowire Electrode," *Science*, **330**(6010), pp. 1515–1520.
- [308] Karki, K., Epstein, E., Cho, J.-H., Jia, Z., Li, T., Picraux, S. T., Wang, C., and Cumings, J., 2012, "Lithium-Assisted Electrochemical Welding in Silicon Nanowire Battery Electrodes," *Nano Lett.*, **12**(3), pp. 1392–1397.
- [309] McDowell, M. T., Lee, S. W., Nix, W. D., and Cui, Y., 2013, "25th Anniversary Article: Understanding the Lithiation of Silicon and Other Alloying Anodes for Lithium-Ion Batteries," *Adv. Mater.*, **25**(36), pp. 4966–4985.
- [310] Liu, X. H., Wang, J. W., Huang, S., Fan, F., Huang, X., Liu, Y., Krylyuk, S., Yoo, J., Dayeh, S. A., Davydov, A. V., Mao, S. X., Picraux, S. T., Zhang, S., Li, J., Zhu, T., and Huang, J. Y., 2012, "In Situ Atomic-Scale Imaging of Electrochemical Lithiation in Silicon," *Nat. Nanotechnol.*, **7**, pp. 749–756.
- [311] Liu, X. H., Zheng, H., Zhong, L., Huang, S., Karki, K., Zhang, L. Q., Liu, Y., Kushima, A., Liang, W. T., Wang, J. W., Cho, J.-H., Epstein, E., Dayeh, S. A., Picraux, S. T., Zhu, T., Li, J., Sullivan, J. P., Cumings, J., Wang, C., Mao, S. X., Ye, Z. Z., Zhang, S., and Huang, J. Y., 2011, "Anisotropic Swelling and Fracture of Silicon Nanowires During Lithiation," *Nano Lett.*, **11**(8), pp. 3312–3318.
- [312] Chen, J., Conache, G., Pistol, M.-E., Gray, S. M., Borgström, M. T., Xu, H., Xu, H. Q., Samuelson, L., and Håkanson, U., 2010, "Probing Strain in Bent Semiconductor Nanowires With Raman Spectroscopy," *Nano Lett.*, **10**(4), pp. 1280–1286.
- [313] Han, X., Kou, L., Lang, X., Xia, J., Wang, N., Qin, R., Lu, J., Xu, J., Liao, Z., Zhang, X., Shan, X., Song, X., Gao, J., Guo, W., and Yu, D., 2009, "Electronic and Mechanical Coupling in Bent ZnO Nanowires," *Adv. Mater.*, **21**(48), pp. 4937–4941.
- [314] Wei, B., Zheng, K., Ji, Y., Zhang, Y., Zhang, Z., and Han, X., 2012, "Size-Dependent Bandgap Modulation of ZnO Nanowires by Tensile Strain," *Nano Lett.*, **12**(9), pp. 4595–4599.
- [315] Sun, L., Kim, D. H., Oh, K. H., and Agarwal, R., 2013, "Strain-Induced Large Exciton Energy Shifts in Buckled CdS Nanowires," *Nano Lett.*, **13**(8), pp. 3836–3842.
- [316] Campbell, G. H., McKeown, J. T., and Santala, M. K., 2014, "Time Resolved Electron Microscopy for In Situ Experiments," *Appl. Phys. Rev.*, **1**(4), p. 41101.
- [317] Kim, J. S., Lagrange, T., Reed, B. W., Taheri, M. L., Armstrong, M. R., King, W. E., Browning, N. D., and Campbell, G. H., 2008, "Imaging of Transient Structures Using Nanosecond In Situ TEM," *Science*, **321**(5895), pp. 1472–1475.
- [318] Xu, F., Durham, J. W., Wiley, B. J., and Zhu, Y., 2011, "Strain-Release Assembly of Nanowires on Stretchable Substrates," *ACS Nano*, **5**(2), pp. 1556–1563.
- [319] Cao, Z., Tao, L., Akinwande, D., Huang, R., and Liechti, K. M., 2015, "Mixed-Mode Interactions Between Graphene and Substrates by Blister Tests," *ASME J. Appl. Mech.*, **82**(8), p. 081008.
- [320] Feng, X., Meitl, M. A., Bowen, A. M., Huang, Y., Nuzzo, R. G., and Rogers, J. A., 2007, "Competing Fracture in Kinetically Controlled Transfer Printing," *Langmuir*, **23**(25), pp. 12555–12560.
- [321] Meitl, M. A., Zhu, Z. T., Kumar, V., Lee, K. J., Feng, X., Huang, Y. Y., Adevsida, I., Nuzzo, R. G., and Rogers, J. A., 2006, "Transfer Printing by Kinetic Control of Adhesion to an Elastomeric Stamp," *Nat. Mater.*, **5**, pp. 33–38.
- [322] Liu, X., Long, Y.-Z., Liao, L., Duan, X., and Fan, Z., 2012, "Large-Scale Integration of Semiconductor Nanowires for High-Performance Flexible Electronics," *ACS Nano*, **6**(3), pp. 1888–9000.
- [323] Schaedler, T. A., Jacobsen, A. J., Torrents, A., Sorensen, A. E., Lian, J., Greer, J. R., Valdevit, L., and Carter, W. B., 2011, "Ultralight Metallic Microlattices," *Science*, **334**(6058), pp. 962–965.
- [324] Meza, L. R., Das, S., and Greer, J. R., 2014, "Strong, Lightweight, and Recoverable Three-Dimensional Ceramic Nanolattices," *Science*, **345**(6202), pp. 1322–1326.
- [325] Zheng, X., Lee, H., Weisgraber, T. H., Shusteff, M., DeOtte, J., Duoss, E. B., Kuntz, J. D., Biener, M. M., Ge, Q., Jackson, J. A., Kucheyev, S. O., Fang, N. X., and Spadaccini, C. M., 2014, "Ultralight, Ultrastiff Mechanical Metamaterials," *Science*, **344**(6190), pp. 1373–1377.
- [326] Bhushan, B., and Marti, O., 2010, *Scanning Probe Microscopy—Principle of Operation, Instrumentation, and Probes* (Springer Handbook of Nanotechnology), Springer, Berlin, pp. 573–617.
- [327] Yuya, P. A., Hurley, D. C., and Turner, J. A., 2008, "Contact-Resonance Atomic Force Microscopy for Viscoelasticity," *J. Appl. Phys.*, **104**(7), p. 74916.
- [328] Gao, H., Ji, B., Jager, I. L., Arzt, E., and Fratzl, P., 2003, "Materials Become Insensitive to Flaws at Nanoscale: Lessons From Nature," *Proc. Natl. Acad. Sci. U.S.A.*, **100**(10), pp. 5597–5600.